



ISTITUTO NAZIONALE DI FISICA NUCLEARE
(LNF) Laboratori Nazionali di Frascati

INFN-20-16/LNF

04 Novembre 2020

Asymmetric Elastoplastic Behavior and Failure of GEM Foils

Guido Raffone[†]

INFN, Laboratori Nazionali di Frascati, P.O. Box 13, I-00044 Frascati (RM), Italy

[†]*mailto: guido.raffone@lnf.infn.it*

Abstract

The *nonlinear isotropic power hardening* and the *cohesive zone material (CZM)* [1] criteria are applied in ANSYS® [2] finite element simulations to analyze very large deformations of the GEM foils up to the failure in uniaxial tensile tests. Some data available in literature concerning both the PI/Cu and the grain boundary interfaces are utilized. The computed progressive plasticization of the perforated thin multilayer agree very well with the experimental results published by some researchers [3–6]. However the present work provides a different explanation of that behavior (already suggested in an earlier note of the author [7]) and it should be considered as a critical review concerning the conclusions of the aforementioned works.

Keywords: thin films, polymers, cohesive zone material, adhesion, grain boundaries.

*Published by
Laboratori Nazionali di Frascati*

1 Introduction

A GEM foil [8,9] is a double side micro-perforated polyimide (PI) (e.g. Kapton®) flexible copper clad laminate (FCCL); it is the fundamental element of a new generation of HEP detectors and its performance make itself attractive for other applications as medical imaging. Even if the working conditions of a large area GEM foil are usually not critical, several tensile tests were carried out in the plastic region [3–6] to investigate the stretching technique limits, the holes deformations, the radiation damage and the moisture effect. The plasticization process of a PI/Cu multilayer is very complex and the hexagonal perforation pattern of the GEM foil adds another difficulty making it asymmetric; a standard approach [10] usually requires a preliminary investigation on the bulk materials, the surface and the film microstructure (FIB, SEM, TEM) other than the Young modulus (partial relief, indentation, bulge), the residual stress (x-ray, bulge), the thickness (microscopy), the cracks generation (electrical resistance) and the adhesion (4 PB, DCB, LS). As far as the author knows the majority of the tests on GEM foils are devoted to the holes geometry acceptance because of the electrons avalanche [11] but there are only a few information on the mechanical properties that must be deduced in another way. For instance the metal film microstructure of these foils ($h_f = 2 - 5\mu m$) as well as the interface adhesion depend mainly on the sputtering deposition on the PI substrate ($h_s = 50 - 70\mu m$); also the subsequent chemical perforation etchings ($\phi = 30 - 70\mu m$) in an hexagonal pattern ($p = 140\mu m$) affect the copper layer texture other than the overall mechanical weakening; the same for annealing and surface treatment. As example playing with the RF sputtering power [12] allows a grains columnar growth making the laminate extremely stretchable if compared to an equiaxed grain structure that usually has higher strength. Recently [15] the Hall-Petch constants for Cu thin films have been updated taking into account the type of the Cu grain other than its mean size d_G .

Table 1: GEM Cu film yield stress $\sigma_{Y_{0.2\%}}^f$ ($h_f = 5\mu m$; $d_G = 2\mu m$).

<i>Yu-Spaepen</i> (2004) [13] $\sigma_{Y_{0.2\%}}^f = \sigma_0 + kh_f^{-n} = 282 \text{ MPa}$	$\sigma_0 = 116 \text{ MPa}$ $k = 355 \text{ MPa}\mu m^n$ $n = 0.473$	
<i>Xiang-Vlassak</i> (2006) [14] ^a $\sigma_{Y_{0.2\%}}^f = \sigma_0 + kd_G^{-n} = 176 \text{ MPa}$	$\sigma_0 = 42 \text{ MPa}$ $k = 190 \text{ MPa}\mu m^n$ $n = 0.5$	
<i>Lee-Ha-Park-Lee</i> (2017) [15] ^b $\sigma_{Y_{0.2\%}}^f = \sigma_0 + kd_G^{-n} + S =$ $= 162 \text{ Mpa columnar}$ $= 189 \text{ Mpa equiaxed}$	<i>columnar</i> $\sigma_0 = 26 \text{ MPa}$ $S = 57 \text{ MPa}$ $k = 112 \text{ MPa}\mu m^n$ $n = 0.5$	<i>equiaxed</i> $\sigma_0 = 26 \text{ MPa}$ $S = 84 \text{ MPa}$ $k = 112 \text{ MPa}\mu m^n$ $n = 0.5$

^a Unpassivated. ^b At room temperature.

The mean grain size d_G of a sputtered film usually does not scale with the film thickness and the grains have a columnar structure equiaxed in the plane of the film [16]; then the yield stress cannot be evaluated by means of the *thickness model* [13] as previously done [7]. The Table 1 emphasizes that discrepancy showing the yield stress for a mean grain size $d_G = 2\mu\text{m}$; the lack of information about the yield increases the computational effort also because of the greater number of unknowns to fit the experimental results. Then, at first sight, a mean grain size range of $d_G = 0.4 - 2\mu\text{m}$ seems a reliable hypothesis because the GEM foils showed a good stretchability during all the tensile tests; the related yield stress range is $\sigma_{Y_{0.2\%}}^f = 176 - 342$ MPa. Due to that uncertainty, the adopted FEM micro-model has also two CZM interfaces; the first for the copper layer to simulate a single crack as proposed in [17, 18]; the second for the Kapton® layer to simulate the channel crack, i.e. the propagation from the Cu to the PI layer of the fracture. In [17, 18] the assumed Cu film yield stress is $\sigma_{Y_{0.2\%}}^f = 100$ MPa as suggested in [19]; conversely, just to remark the above mentioned discrepancy, the *thickness model* [13] gives $\sigma_{Y_{0.2\%}}^f = 937$ MPa ($h_f = 170$ nm) and $\sigma_{Y_{0.2\%}}^f = 321$ MPa ($h_f = 3.2\mu\text{m}$) respectively (in general [15] the Hall-Petch relation is valid up to the nano-scale i.e. a mean grain size d_G of a few hundreds of nm ¹). Then for the GEM copper film the knowledge of the mean grain size d_G evaluated by the intercept method where the twins are counted as separate grains [14] ² is essential even if aimed tests at the yield stress measurement on unperforated multilayer are favored to get proper Hall-Petch coefficients. As well as the yield stress also the Young modulus of the GEM copper film is undetermined and some authors [15] quote even a range of 50 – 90 GPa [15] for electroplated thickness from $h_f = 6\mu\text{m}$ on; also the copper film hardening properties found in literature are not always agreeing too and sometimes refer simply to the bulk ones. Same considerations concern the PI mechanical properties also and some data were retrieved from [6]. Then the setup of the FEM model was obtained making as little compromises as possible rather than aiming a confidence on the estimated parameters, as often happens when the numerical approach is separated from the experimental activity; as previously underlined a huge variety of methods on this subject is available and the increasing support of the simulations in these engineering fields is no more submitted to the experimentation but it is considered as *the other side of the coin*.

This work is substantially divided into two parts. The first one deals with the correlation with the experimental results and the following plastic analysis shows clearly the asymmetric evolution of the deformation of the GEM foils; it did not give particular difficulties and the congruity is fine. The second one is much more challenging since it tries to study the failure (undoubtedly originated from a hole) by simulating the coupled effects of adhesion and crack propagation; it is more demanding as far as the computational effort and the presented results are very preliminary.

¹Under a few tens of nm the *inverse Hall-Petch effect* is observed.

²The twins are considered as grain boundaries providing a much smaller averaged size.

2 Part I: The asymmetric plasticization of the GEM foils.

In most of the herein referenced works both the Kapton® and the copper layers are considered elastoplastic materials, the former steeply and the latter weakly hardening, following a power law after the yield and obeying to the J_2 flow theory.

$$\begin{cases} \sigma^{f,s} = E_{f,s}\epsilon & \text{if } \epsilon \leq \sigma_Y^{f,s}/E_{f,s} \\ \sigma^{f,s} = \sigma_Y^{f,s} (E_{f,s}\epsilon/\sigma_Y^{f,s})^{N_{f,s}} & \text{if } \epsilon > \sigma_Y^{f,s}/E_{f,s} \text{ where } 0 \leq N_{f,s} \leq 1 \end{cases} \quad (1)$$

In the equation 1 the sub/super-scripts f, s stand for *film* and *substrate* respectively; the hardening exponent $N_{f,s} = 0$ corresponds to an *elastic-perfectly plastic* behavior and $N_{f,s} = 1$ to a *purely elastic*; this model is often adopted for large strains in ductile plasticity; some authors include the viscoelastic features for the polymer which is useless in the present case because the GEM foil failure occurs at relatively low strains; for this reason the data points exceeding 0.2 total plastic strain were excluded from the fitting.

2.1 Dry non-irradiated Kapton® HN foils hardening properties fit.

Experimental data were retrieved from [5,6] for the dry non-irradiated tests only; a first fit is obtained keeping the Young modulus $E_s = 2385$ MPa from [6] as a constant and the exponent $N_s = 0.58$ is determined by matching the yield $\sigma_{Y_{3\%}}^s = 69$ MPa taken from [20] as shown in Fig. 1.

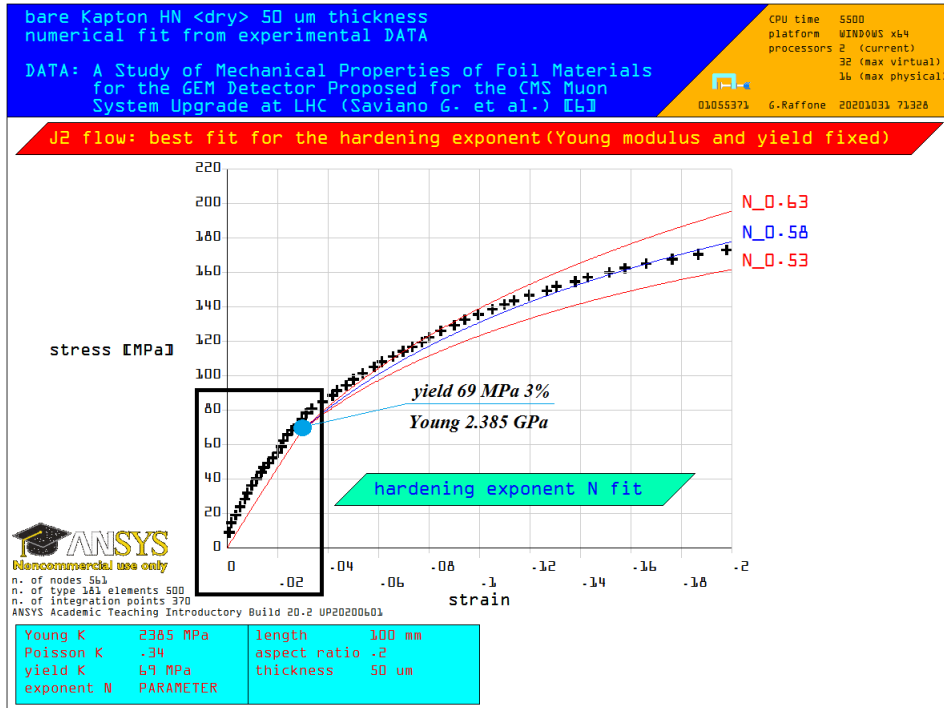


Figure 1: Dry non-irradiated Kapton® HN 50 μ m best hardening exponent $N_s = 0.58$; Young $E_s = 2385$ MPa and yield stress $\sigma_{Y_{3\%}}^s = 69$ MPa fixed; DATA points in [5,6].

A better fit (Fig. 2) is achieved by adjusting one parameter of the three E_s , σ_Y^s , N_s , at a time; the explored ranges are $N_s = 0.50 - 0.60$, $\sigma_Y^s = 40 - 60$ MPa (Fig. 3) and $E_s = 2400 - 4400$ MPa (Fig. 4) for the exponent, the yield and the Young respectively; a hardening exponent $N_s = 0.55$ ³, a Young modulus $E_s = 3400$ MPa⁴ and a yield stress $\sigma_{Y_{1.5\%}}^s = 50$ MPa match very well the experimental data; the Young modulus $E_s = 3400$ MPa is much higher than $E_s = 2385$ MPa⁵ computed in [6]; that discrepancy is due to that any PI never shows a clear transition to plasticity leading to both ambiguous interpretations of data and erroneous experimental procedures; for instance the partial unloading practice to extract the elastic constants is usually adopted by a lot of authors [13,14,16]; other authors [17–19] set a value of $E_s = 8$ GPa for similar analysis with a yield $\sigma_Y^s = 50$ MPa denoting a very low strain plasticization; the Young $E_s = 3400$ MPa was previously adopted in [7] since referenced in [13] with a fifth-order polynomial fit accuracy.

In the present case the choice of an higher Young modulus E_s forces the assumption of a lower yield stress σ_Y^s diminishing the transition to plasticity from 3% to 1.5% strain.

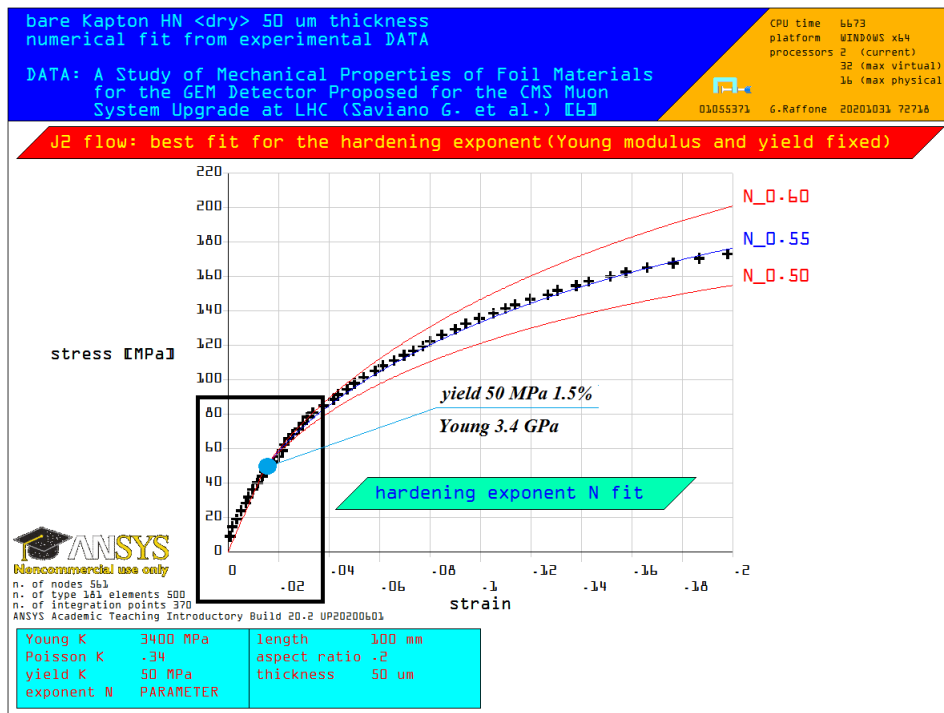


Figure 2: Dry non-irradiated Kapton® HN 50 μ m best hardening exponent $N_s = 0.55$; Young $E_s = 3400$ MPa and yield stress $\sigma_{Y_{1.5\%}}^s = 50$ MPa fixed; DATA points in [5,6].

³An exponent $N_s = 0.50$ is widely used in literature for PI films.

⁴In the DuPont™ data-sheet [20] (2019) $E_s = 2.76$ GPa and in older ones $E_s = 2.5$ GPa.

⁵That averaged value looks like a *secant* rather than an *elastic* modulus; also the computed Young modulus of the GEM foils (dry and non-irradiated) $E_{GEM} = 6.026$ GPa in [6] is highly underestimated since corresponds to an extremely low copper film Young modulus $E_f = 45.8$ GPa.

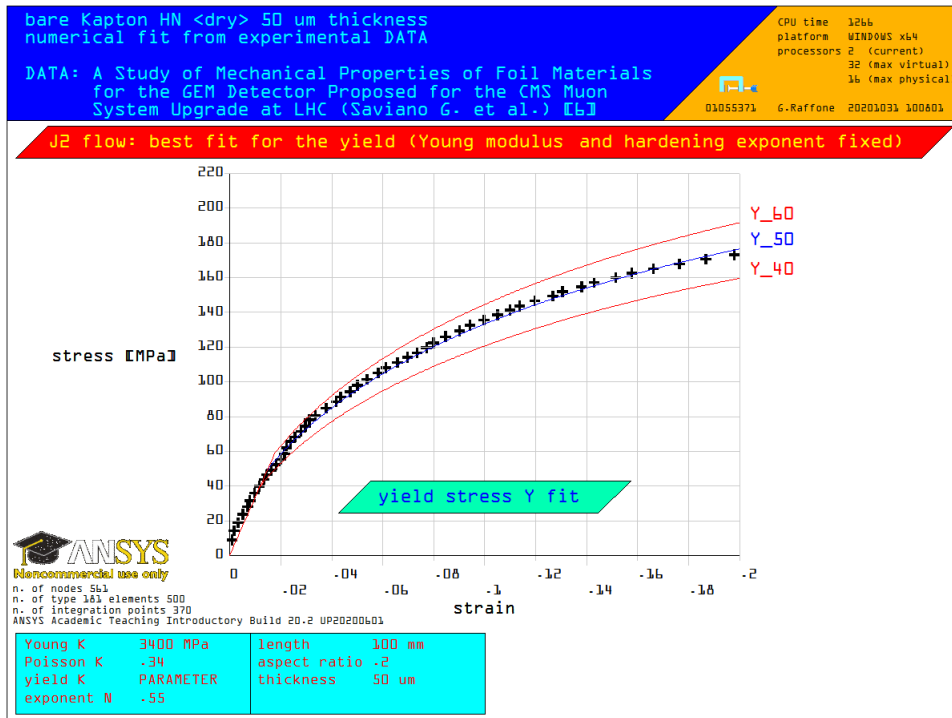


Figure 3: Dry non-irradiated Kapton® HN 50µm best yield stress $\sigma_{Y_{1.5\%}}^s = 50$ MPa; Young $E_s = 3400$ MPa and hardening exponent $N_s = 0.55$ fixed; DATA points in [5, 6].

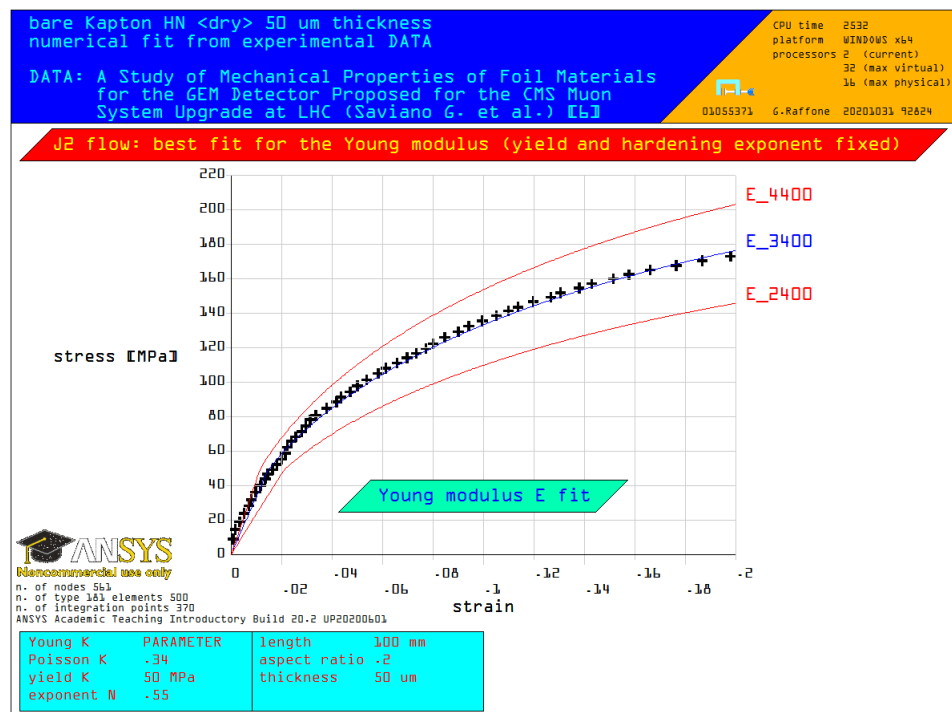


Figure 4: Dry non-irradiated Kapton® HN 50µm best Young $E_s = 3400$ MPa; yield stress $\sigma_{Y_{1.5\%}}^s = 50$ MPa and hardening exponent $N_s = 0.55$ fixed; DATA points in [5, 6].

Table 2 summarize the parameters (Poisson $\nu_s = 0.34$) that will be adopted in the FEM micro-model of the next sections.

Table 2: Dry non-irradiated Kapton® HN 50 μ m best fit results.

Young modulus E_s [GPa]	yield stress $\sigma_{Y_{1.5\%}}^s$ [MPa]	hardening exponent N_s
3.4	50.0	0.55

2.2 The asymmetry of the SCFs and of the geometry in the GEMs.

The different holes pitch (namely *short* and *long*) due to the hexagonal symmetry of a GEM foil leads to very different stress fields depending on the tensile direction [7]; Fig. 5 shows the computed uniaxial SCFs ⁶ $K_x^0 = -0.76$, $K_x^{\pi/2} = +4.24$, $K_y^0 = +3.34$ and $K_y^{\pi/2} = -1.72$ where the superscripts is the location ($\theta = 0$ or $\theta = \pi/2$) and the subscript is the tensile direction (x or y) in very good agreement with [21] for a ligament efficiency of 0.5; they are much greater than those of a single hole in an infinite plate.

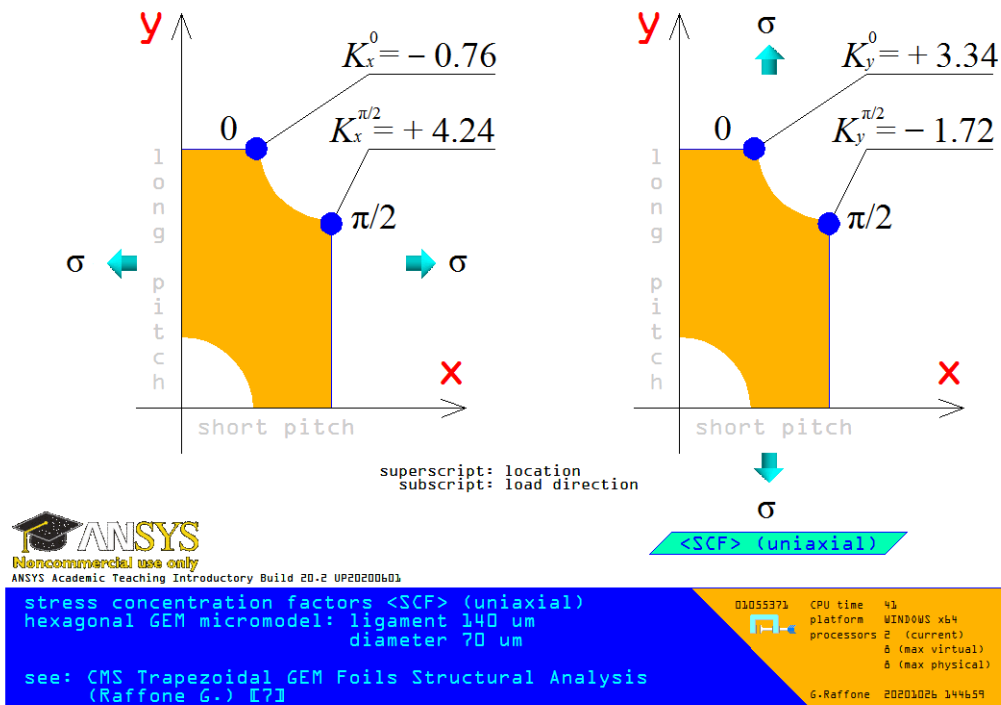


Figure 5: SCFs asymmetry due to the hexagonal pattern of a GEM foil.

⁶Stress Concentration Factor(s).

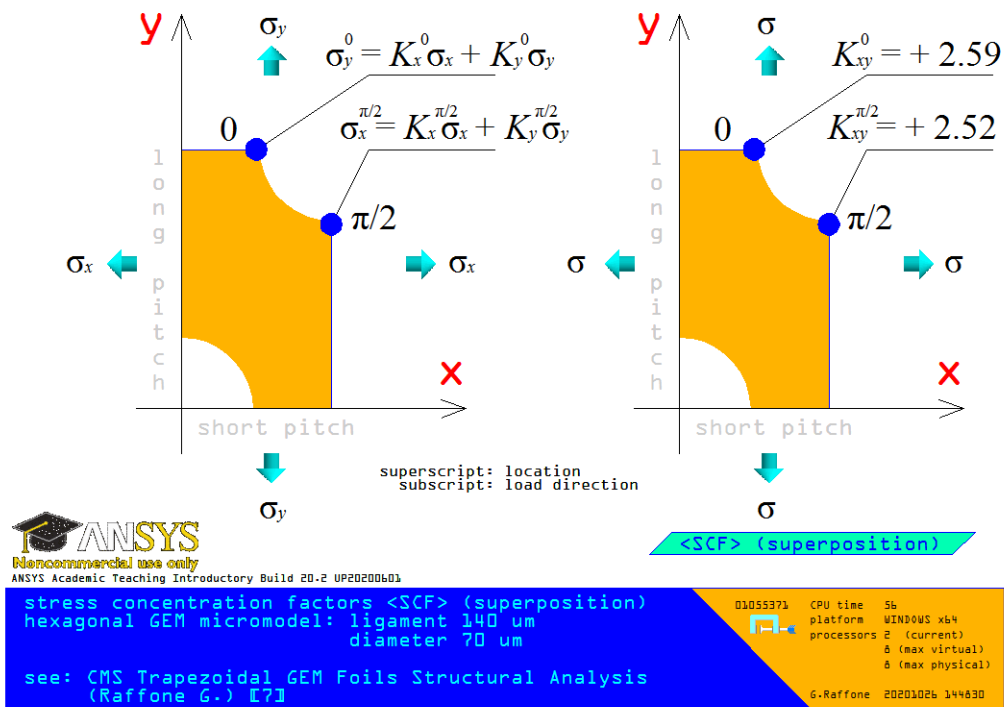


Figure 6: General superposition of the SCFs; on the right the biaxial superposition.

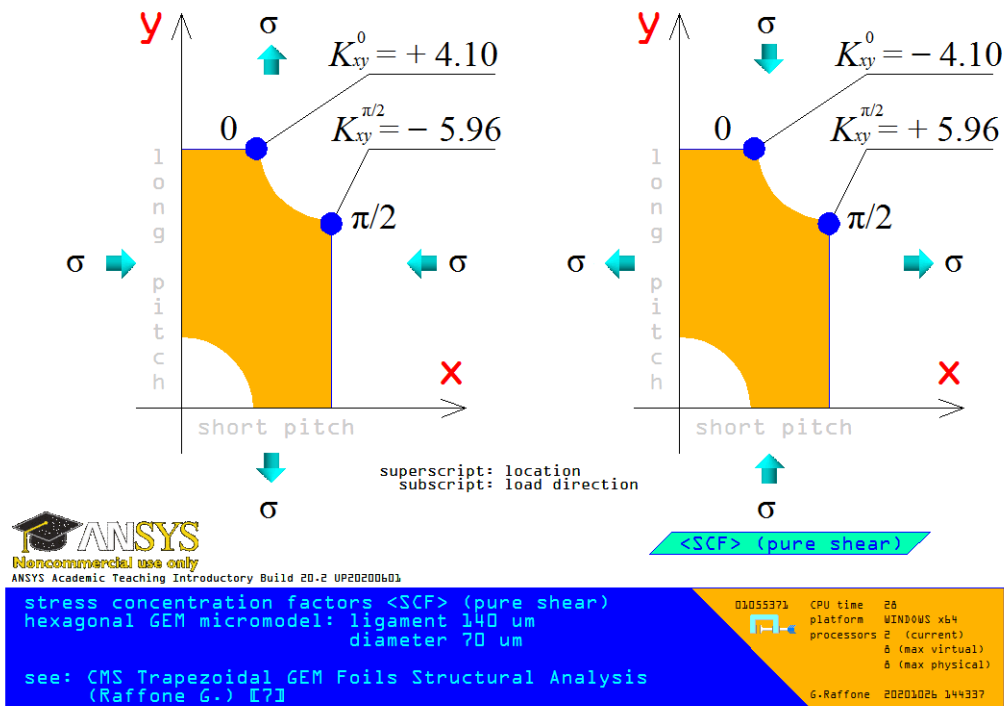


Figure 7: Pure shear SCFs.

The *superposition principle* (Fig. 6) clearly implies that any biaxial stretching like the thermal one [22] is better anyway; moreover (Fig. 5) the tensile SCF is greater if stretching along the *short pitch* direction and conversely the compressive SCF is greater if stretching along the *long pitch* direction, in despite of the *macroscopic isotropy*; for the *short pitch* (on the left) $\sigma_x^0 = \sigma_y^{\pi/2} = 0$ and for the *long pitch* (on the right) $\sigma_x^{\pi/2} = \sigma_y^0 = 0$; in both cases the shear τ_{xy}^θ does not vanish for any θ angle but only at $\theta = 0$ and $\theta = \pi/2$ (i.e. $\tau_{xy}^0 = \tau_{xy}^{\pi/2} = 0$)⁷; the high compressive stress at $\theta = 0$ (*short*) and $\theta = \pi/2$ (*long*) may lead to an initial coupled delamination and buckling of the film. In general the cracks are always originated at the points of stress concentration and higher SCFs lead to their early births; the following plasticization process redistributes the stresses around the holes and the asymmetry of the SCFs becomes less and less pronounced but somewhere some cracks are growing till the final failure; then the collapse depends not only on the SCFs but also on the fracture path length between two nearby holes. Therefore in GEMs foils there are mainly two kinds of asymmetry: the first is *purely geometrical* (*short* and *long pitch*) and the second is *purely mechanical* (the SCFs); they are the only asymmetries related to both the hole deformation and the failure observed in the above mentioned tests; any other interpretation like the HV partitions effect [4] and their spacing is contradictory because the SCFs asymmetry leads to different load-strain curves and the geometrical asymmetry leads to different crack path lengths⁸.

2.3 Dry non-irradiated GEM foils hardening properties fit.

Following the same procedure of of 2.1 also the hardening properties of the copper film of the GEM foil were obtained as Table 4 shows; the plastic FEM micro-model exhibits a remarkable sensitivity to both the yield stress $\sigma_{Y_{0.2\%}}^f$ and the hardening exponent N^f and a lesser to the Young modulus E_f .

Table 3: Dry non-irradiated GEM foils 5/50/5 μ m best fit results.

Young modulus E_f [GPa]	yield stress $\sigma_{Y_{0.2\%}}^f$ [MPa]	hardening exponent N_f
90.	300.	0.11

⁷Conversely the shear vanish on the edge for any θ in the case on a single hole in an infinite plate.

⁸An HVP section (unperforated single side coated 1mm wide) has an equivalent Young modulus E_{HVP} of the same order of magnitude of that of perforated GEM E_{GEM} : $E_{HVP} = 50/55E_s + 5/55E_f = 11.27$ GPa (*rule of mixtures*, $E_s = 3.4$ GPa, $E_f = 90$ GPa) and $E_{GEM} = 9.44$ GPa; then an HVP section deforms 0.84 times the GEM only; moreover in both the sections the metal film carries most of the tensile load because the copper is much more rigid than the Kapton® ($E_f/E_s = 26.5$) and roughly the film of the single side coated has twice the stress of the film of the double side coated; more precisely the mean stress of the HVP section copper layer is 1.73 times that of the GEM film without taking into account the SCF multiplier; assuming a SCF of 3.34 for the GEM film (*long pitch* stretching) the resulting mean stress of the HVP section copper layer is 0.52 times the maximum stress of the GEM film, i.e. a failure is expected from a crack initiated in a hole (brittle like) rather than in an HVP section (ductile necking); in the *short pitch* stretching the SCF is 4.24 and that factor goes down to 0.41.

The yield stress $\sigma_{Y_{0.2\%}}^f = 300$ MPa corresponds to a mean grain size $d_G = 0.54\mu\text{m}$; it is a very high yield greater than that given by the *thickness model* [13] unveiling a very good quality of the sputter deposition of such a relatively thick film thickness; the estimated Young modulus $E_f = 90$ GPa is lower than the value 108.8 GPa previously assumed [7, 13]⁹. The hardening exponent $N^f = 0.11$ is very different from the value of 0.02 adopted in [17–19] but agree very well with [16]¹⁰. Fig. 8 shows two different load-strain curves for the GEM foils, the upper for the *long pitch* stretching and the lower for the *short pitch* stretching as expected; the curves do not end with a failure but rise indefinitely and describe the plastic evolution only; the remarkable difference between the two curves is due to the initial strong asymmetry of the SCFs¹¹. The fit criterion simply includes inside these two curves all the collected experimental data retrieved from [4] as shown in Fig. 9 (samples with HVP, presumably *long pitch*) and in Fig. 10 (samples without HVP, presumably *short pitch*) since there is no information about the orientation of the fit. As above mentioned there are many triplets $E_{f,s}, \sigma_Y^{f,s}, N_{f,s}$ giving even better fits and that kind of simulation assume significance only removing the uncertainties concerning the assumed parameters.

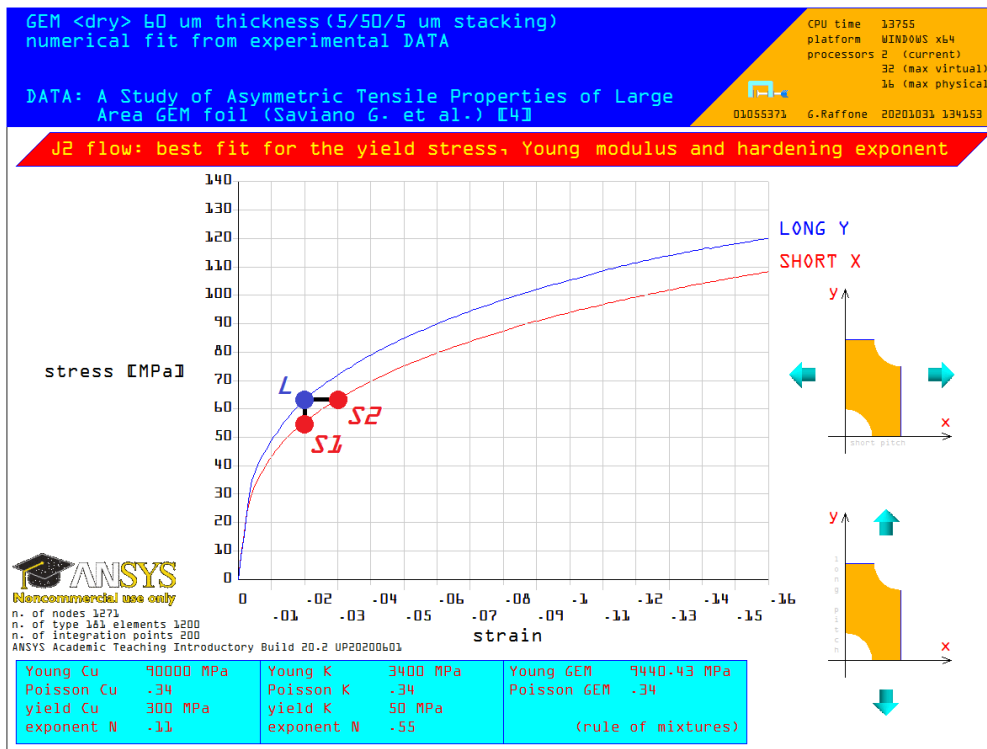


Figure 8: Unequal load-strain curves due to the SCFs asymmetry.

⁹If $E_f = 90$ GPa and $E_s = 3.4$ GPa assuming a PI volume fraction $\alpha = 5/6$ and a perforation factor of 0.52937 [7, 21] then $E_{GEM} = 9.44$ GPa very close to [3] also; the estimation of the Young of the film E_f is much more important than that of the substrate E_s since $\Delta E_{GEM} \approx -E_f \Delta \alpha$ as $E_f \gg E_s$.

¹⁰That work underlines also the very important and dramatic *Bauschinger effect* due to the passivation.

¹¹The SCFs asymmetry both establishes two different *roads* for the following irreversible plasticization process and anticipate or delay the crack formation in one direction rather than the other.

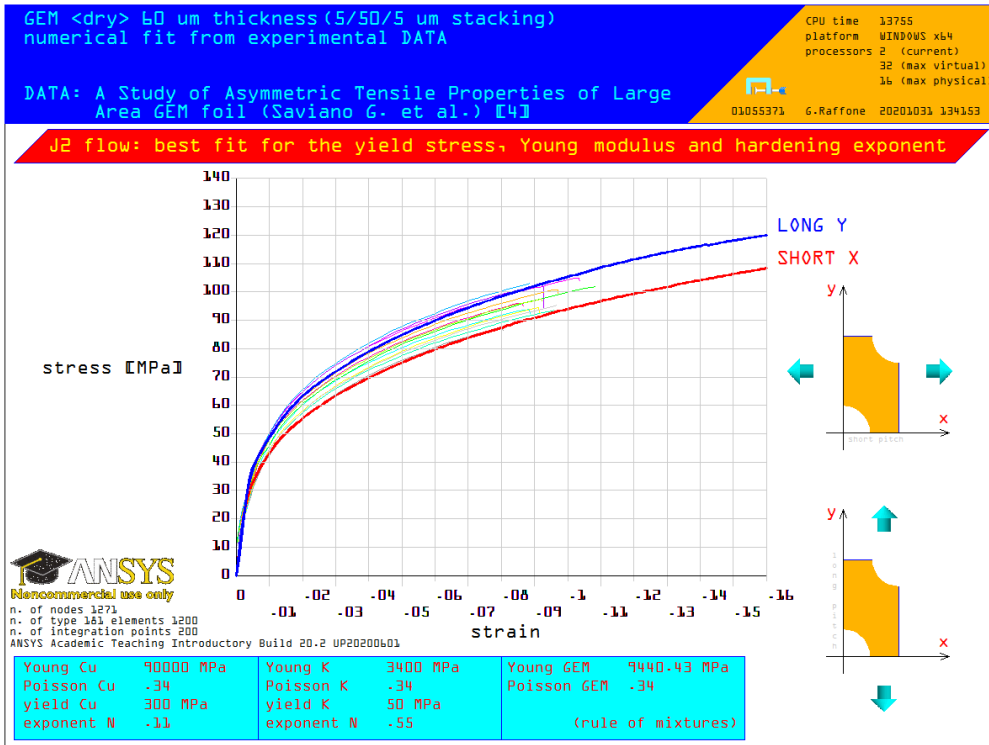


Figure 9: Load-strain curves for specimens with 2 to 5 HVP lines; DATA points in [4].

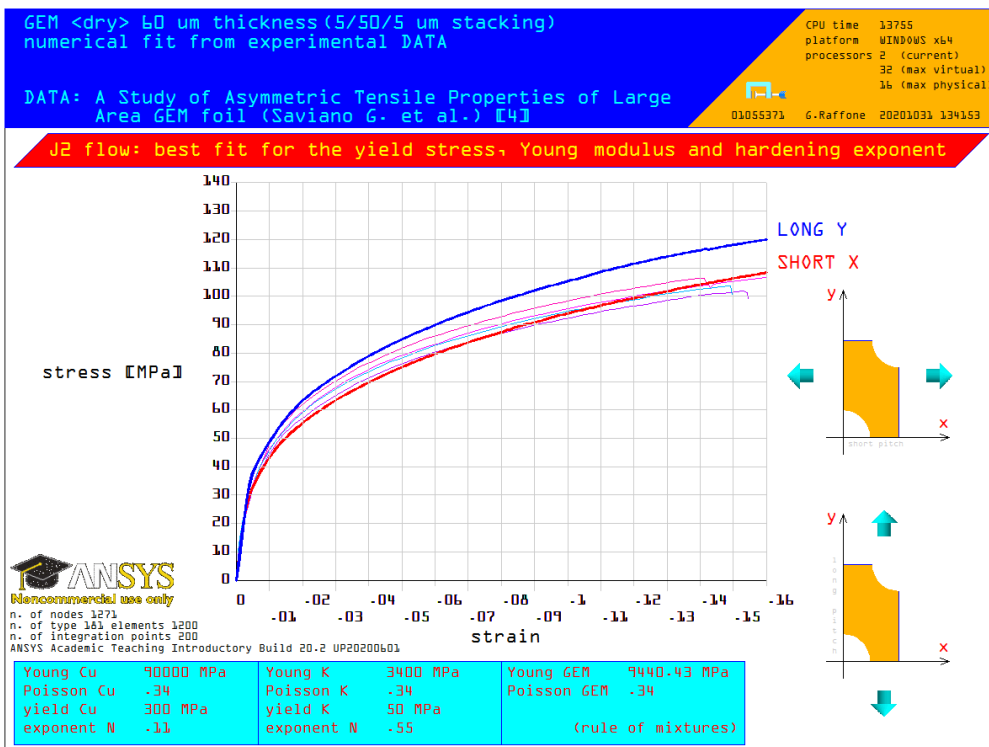


Figure 10: Load-strain curves for specimens without HVP lines; DATA points in [4].

It seems that the experimental load-strain curves in [4] are grouped into two distinct failure strain values, say 0.09 and 0.14, and have dissimilar slopes also; then it is assumed that the failure depends on the direction of the loading and happens at distinct strains by inferring the difference of the two numerical curves of Fig. 8; a hypothesis concerning the unequal strains failures is depicted in Fig. 11.

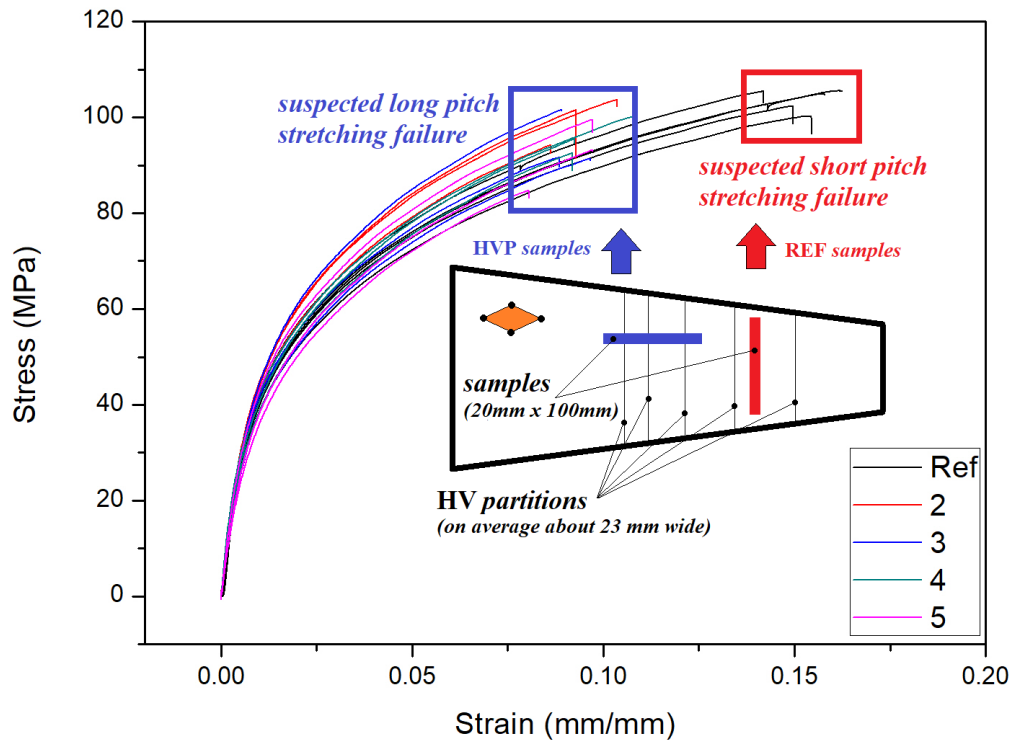


Figure 11: Unequal strains failures (image edited courtesy of [4]).

By making a simple force balance in the *long pitch* direction the applied load to a single perpendicular row of holes is not affected by any of the HVP lines that simply transfer the same load section by section; the number of the HVP lines also has no influence on the "applied load-hole deformation" relation¹². In truth neither the unperforated HV partitions nor their number and distribution have any effect on the hole deformations that depend on both the applied load and the sample orientation only. Fig. 12 shows a very good agreement between the *short pitch* stretching and the samples without HVP lines (the *REF* samples in [4]) as far as the hole deformation; also Fig. 13 shows the same agreement between the *long pitch* stretching and the samples with 2, 3, 4, 5 HVP lines but the longitudinal that does not match absolutely and it is rather curious.

¹²Indeed the results in [4] clearly show that.

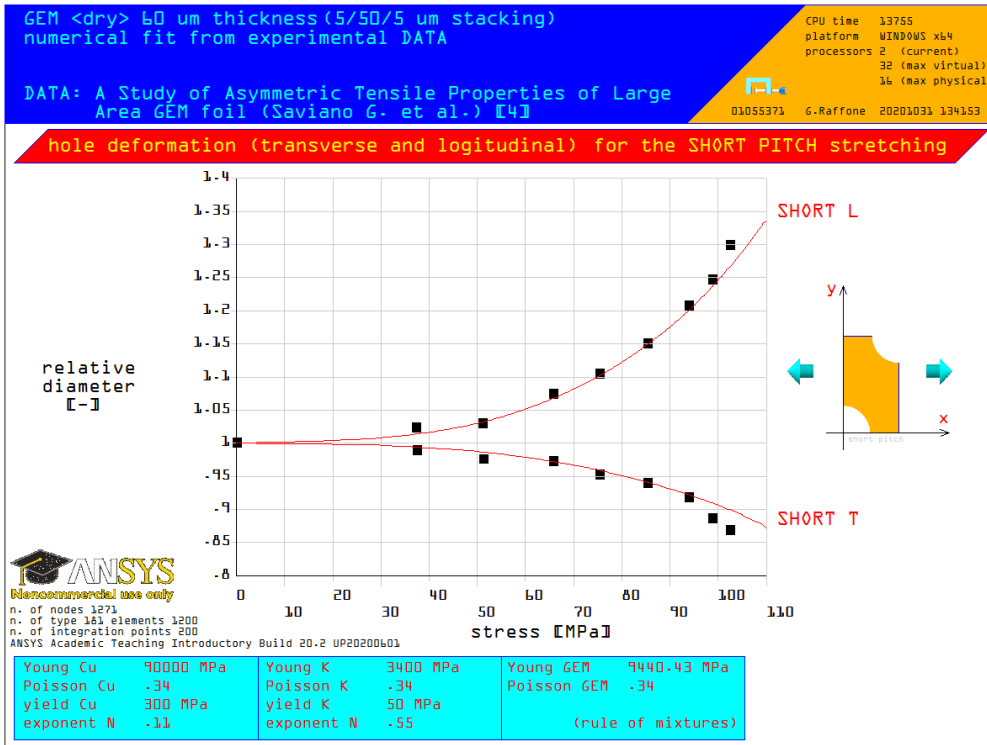


Figure 12: Hole deformation for specimens without HVP lines; DATA points in [4].

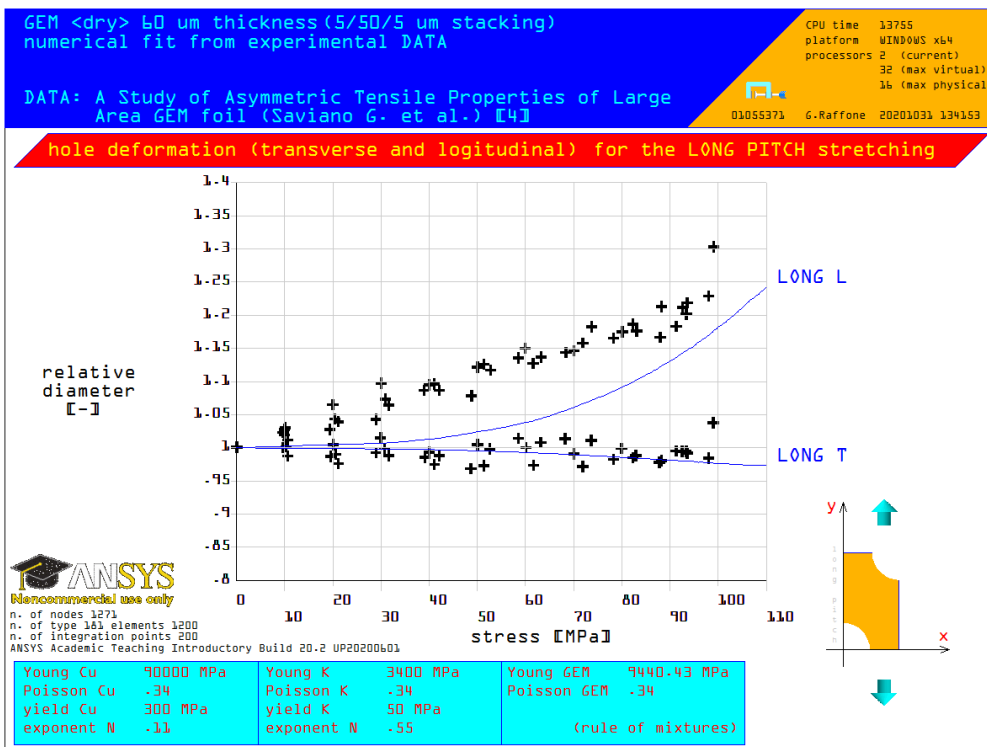


Figure 13: Hole deformation for specimens with 2 to 5 HVP lines; DATA points in [4].

Fig. 14 shows the *peak stress history* of the points 0 and $\pi/2$ (labels *SY00* and *SXPG*) for the *short pitch* stretching of both the copper and Kapton® layers (labels *SHC* and *SHK*); these stresses exceed a lot the ultimate strength of the materials (approximately 230 MPa and 420 MPa¹³ for Kapton® and a very good copper thin film respectively) even at relatively low strains meaning that the fracture originates already at early stages of the stretching; of course these curves are *qualitative* since they both describe the peak stress only and there is no constraint about the failure mechanism; a more representative curve of the mean state of the stress is given by the *SEQV* history related to the *Huber-vonMises-Hencky (HMH)* equivalent stress just in the center *G* (Fig. 15 shows the same history for the *long pitch* stretching).

As expected copper and Kapton® are steeply and weakly hardening respectively and it is manifest the extremely good quality of the bonding of the two layers leading to very high failure strains in despite of that intense stress field¹⁴. For this high level stretching a well bonded Kapton® layer plays a fundamental role [17,23] because inhibits debonding and necking via a complex mechanism of dislocations arrangement¹⁵; radiation and moisture greatly affect the bonding quality and sometimes are the reason of unexpected failures.

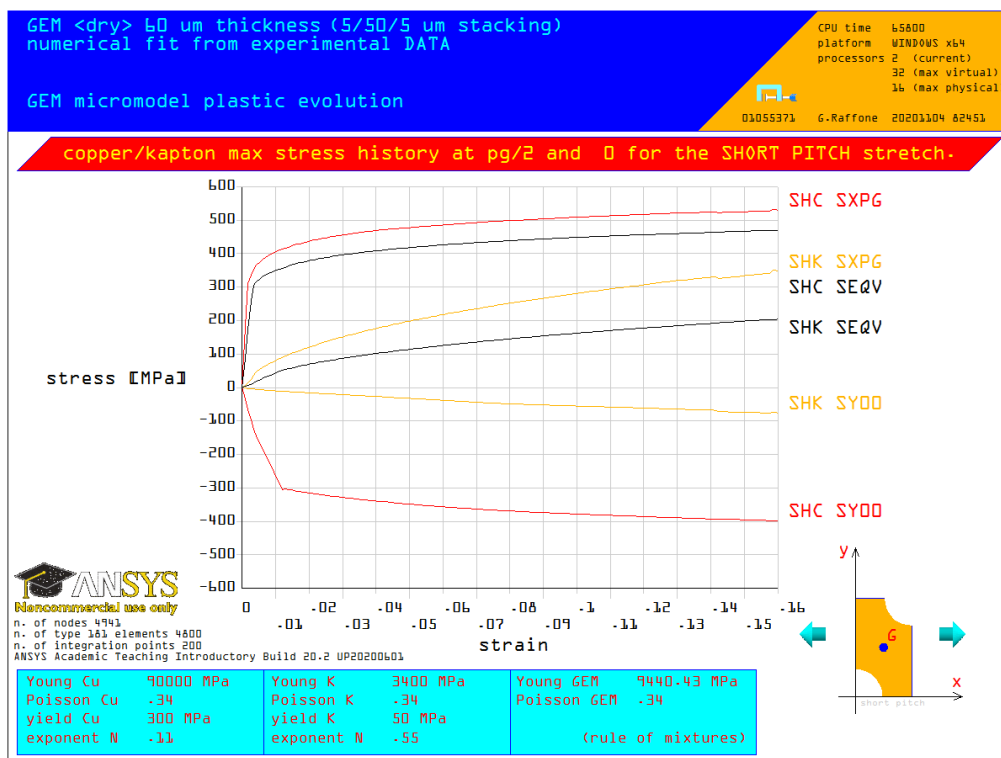


Figure 14: PI/Cu peak stresses at 0 and $\pi/2$ and equivalent stresses (HMH) at *G* for a *short pitch* stretching.

¹³Electrodeposited freestanding 12µm copper films [26] have even greater yield and ultimate stresses.

¹⁴Without perforation the failure strain of that multilayer should be much higher.

¹⁵The polymeric substrates suppress strain localization in metal films and lead to higher stretchability.

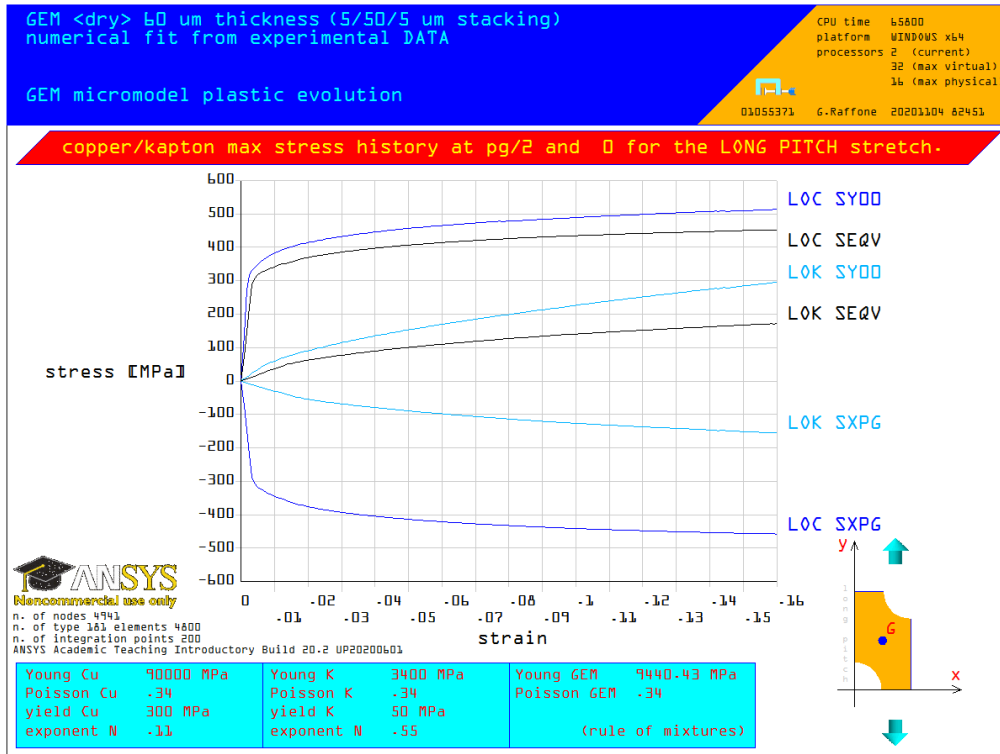


Figure 15: PI/Cu peak stresses at 0 and $\pi/2$ and equivalent stresses (HMH) at G for a long pitch stretching.

Fig. 16 shows the HMH equivalent and peak stresses (tabulated) corresponding to the point L of Fig. 8 (0.02 strain and 63.2 MPa stress for a long pitch stretching); Fig. 17 shows the same values for the point $S1$ (same 0.02 strain of L for a short pitch stretching); Fig. 18 shows again the same values for the point $S2$ (same stress 63.2 MPa of L for a short pitch stretching)¹⁶. What looks rather strange is that the failure for a long pitch stretching happens at strains (say 0.09) lower than those of a short pitch stretching (say 0.14) because the asymmetry of the SCFs implies the contrary ($K_x^{\pi/2} = +4.24 > K_y^0 = +3.34$, Fig. 5), i.e. the short pitch stretching (having a greater SCF) should collapse at strains lower than those of a long pitch stretching if comparing the peak stresses of Figs. 16, 17 and 18. A possible explanation is that the long pitch stretching collapses at lower strains because the fracture path length ($70\mu m$) (i.e. the energy required for the failure) is much lower than the path length of the short pitch stretching ($172\mu m$) as depicted in Fig. 19, i.e. the geometrical asymmetry prevails on the SCFs asymmetry as far as the ultimate failure. That explanation implies that the crack propagation is always perpendicular to the load direction and the fracture mechanism is of mode I only; all the next section conclusions are based on this assumption.

¹⁶For a 0.02 strain the peak stresses are no more proportional to the applied load via the SCFs because of the plasticization; however the difference between the long pitch and short pitch stretching persists as the values at 0 and $\pi/2$ in Figs. 16 and 18 show for the same applied load; it is worthwhile to remember that the applied load must be shared between the layers by virtue of the rule of mixtures.

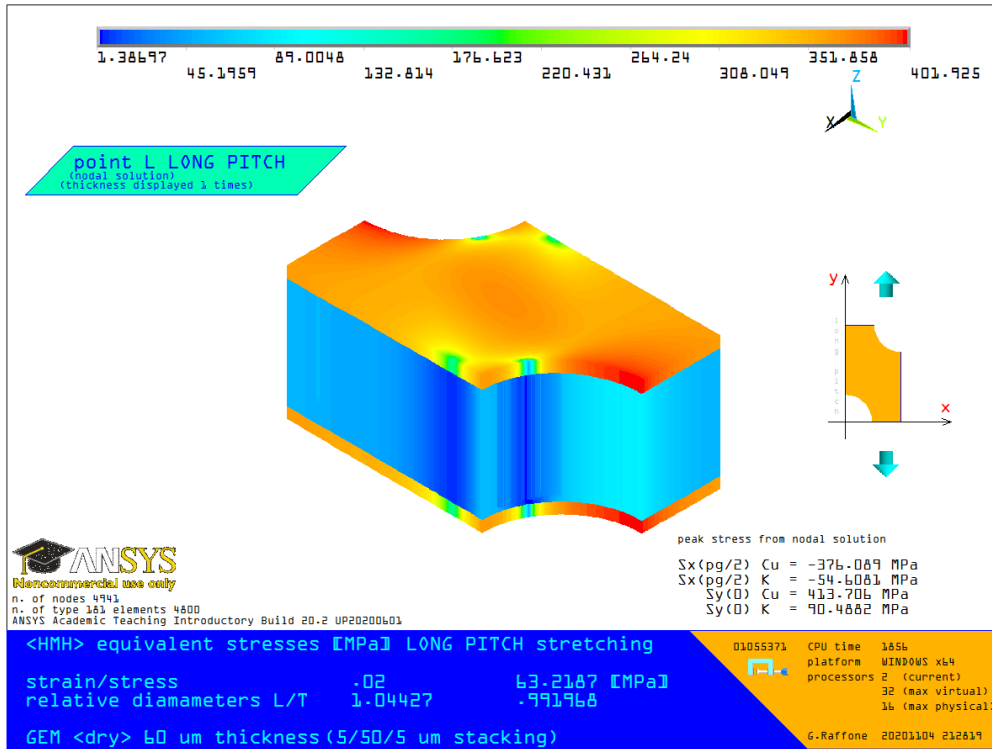


Figure 16: HMH equivalent stress at point L of Fig. 8 (*long pitch stretching*).

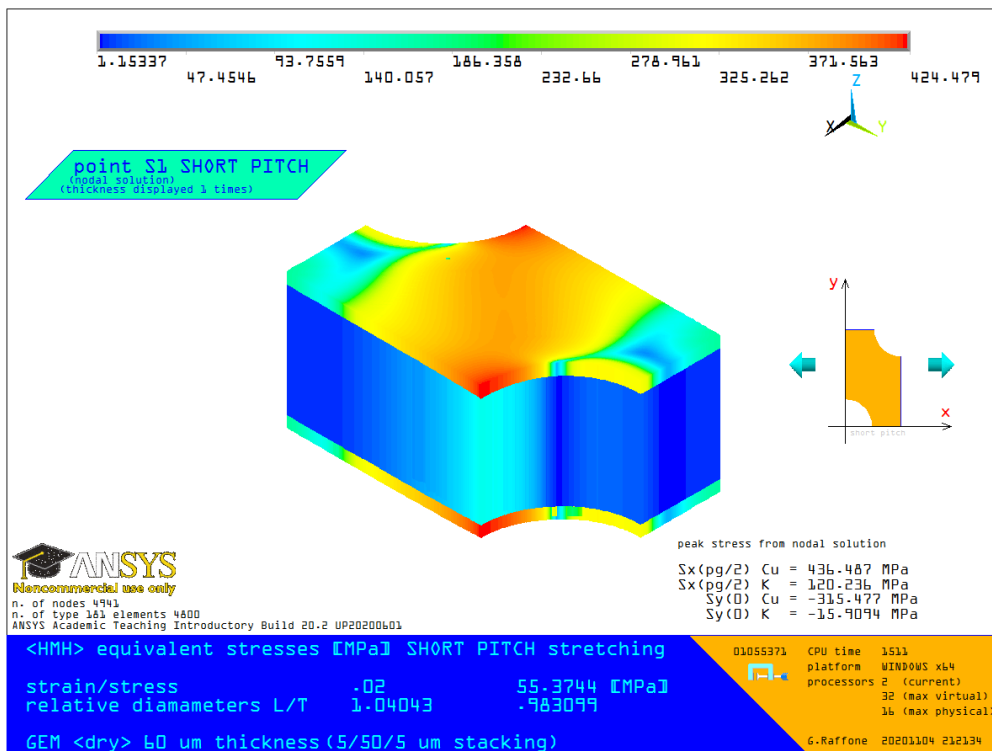


Figure 17: HMH equivalent stress at point $S1$ of Fig. 8 (*short pitch stretching*).

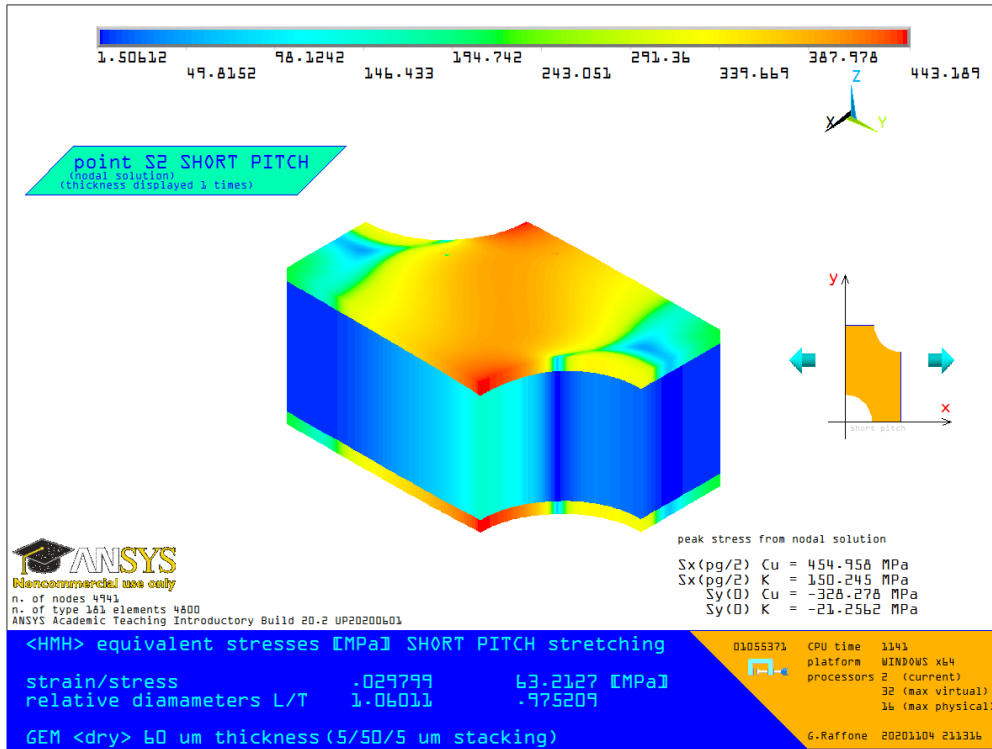


Figure 18: HMH equivalent stress at point $S2$ of Fig. 8 (short pitch stretching).

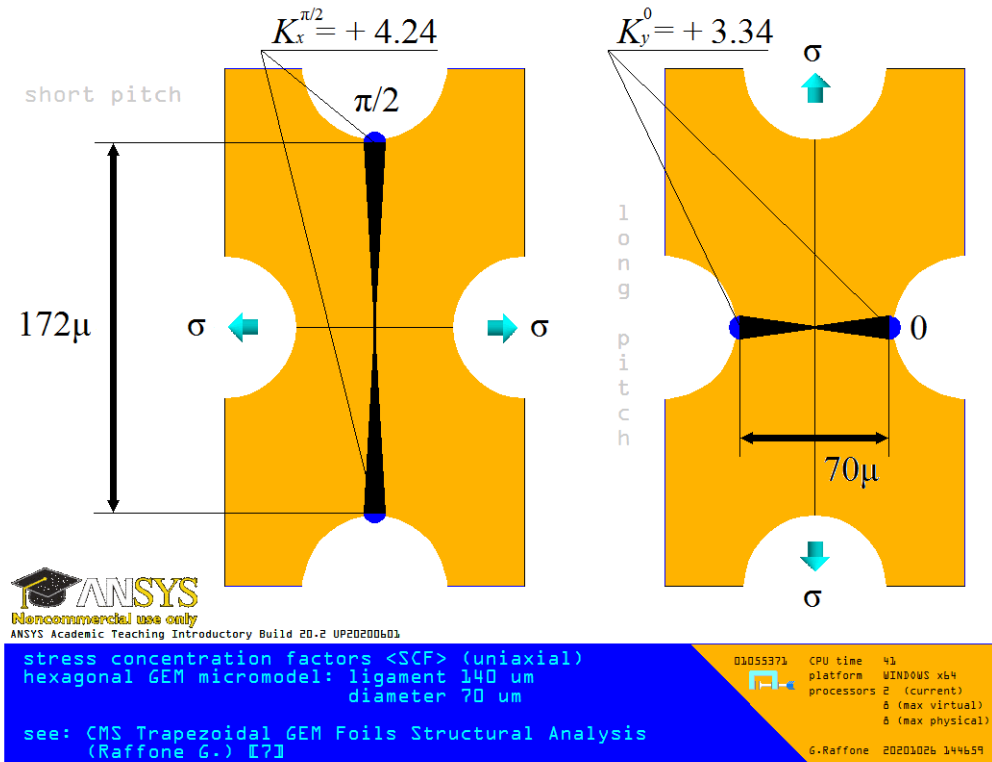


Figure 19: Different crack path lengths.

3 Part II: The CZM model.

Fig. 20 shows the mesh of both the layers (one half of the thickness only, i.e. $25 + 5\mu\text{m}$ of PI+Cu) and three cohesive elements surfaces for the PI/Cu interface (horizontal), the Cu (upper vertical) ¹⁷ and PI (lower vertical) cracks; the coarse mesh is due to the software [2] version; the convergence is sometimes difficult because of the complexity of the model but no *artificial notch* is adopted as other authors do [17, 19] because the hole is a *stress concentrator* itself; in that model the Kapton® hole is not countersunk because it is an ineffective complication since the cracks originate at the free surface of the copper layer.

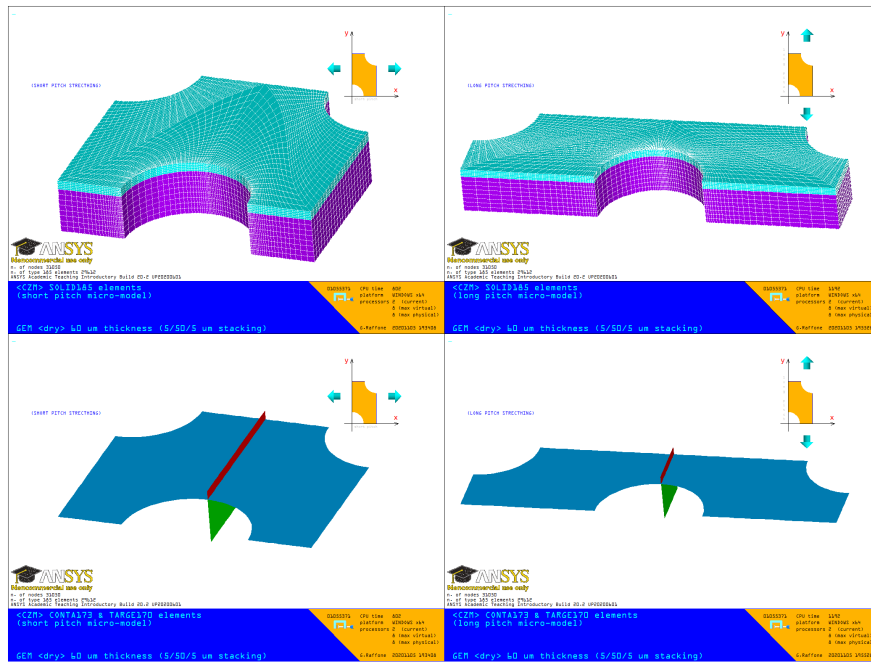


Figure 20: Cohesive Zone Material micro-models for *short* and *long pitch* stretching.

Table 4: *Cohesive Zone Material* model assumed parameters.

interface PI/Cu	$5\mu\text{m}$ copper layer	$50\mu\text{m}$ Kapton® layer
$\sigma_{max}^I = \tau_{max}^I = 150 \text{ MPa}$	$\sigma_{max}^f = 350 \text{ MPa}$	$\sigma_{max}^s = 200 \text{ MPa}$
$\Gamma_{\sigma}^I = \Gamma_{\tau}^I = 1.25 \text{ N/mm}$	$\tau_{max}^f = 0 \text{ MPa}$	$\tau_{max}^s = 0 \text{ MPa}$
	$\Gamma_{\sigma}^f = 5 \text{ N/mm}$	$\Gamma_{\sigma}^s = 4.7 \text{ N/mm}$
	$\Gamma_{\tau}^f = 0 \text{ N/mm}$	$\Gamma_{\tau}^s = 0 \text{ N/mm}$

¹⁷Copper thin films fail by ductile transgranular fracture often with concurrent necking and debonding.

Table 4 summarizes the CZM parameters assumed in the micro-model. The PI/Cu interface peak normal and tangential contact stresses $\sigma_{max}^I = \tau_{max}^I = 150$ MPa [17]¹⁸ and the normalized adhesion energy $\Gamma_{\sigma,\tau}^I E_f / (\sigma_{Y^f})^2 h_f = 250$ [18] correspond to a very good PI/Cu bond strength. The copper interface peak normal stress $\sigma_{max}^f = 350$ MPa is between the yield and the ultimate stress¹⁹; the film fracture energy density $\Gamma_{\sigma}^f = 5$ N/mm corresponds to a copper fracture toughness of 21.2 MPam^{1/2} which is extremely high²⁰. The Kapton® interface peak normal stress $\sigma_{max}^s = 200$ MPa is very close to its ultimate strength and the substrate fracture energy density $\Gamma_{\sigma}^s = 4.7$ N/mm corresponds to a Kapton® fracture toughness of 4.0 MPam^{1/2} much higher than [25] even if other authors assume values up to 6.0 MPam^{1/2}. For both copper and Kapton® interfaces $\tau_{max}^f = \tau_{max}^s = 0$ because of the *mode I* only fracture hypothesis. Then the assumed parameters seem to be very close to the boundaries of the respective materials properties, just not to say they are sometimes exceeding; nevertheless lower values do not fit the experimental curves or lead to convergence instabilities.

The load-strain curve of Fig. 21 shows a clear sharp failure for the *long pitch* stretching at about 0.085 strain and a very good fit with experimental results again.

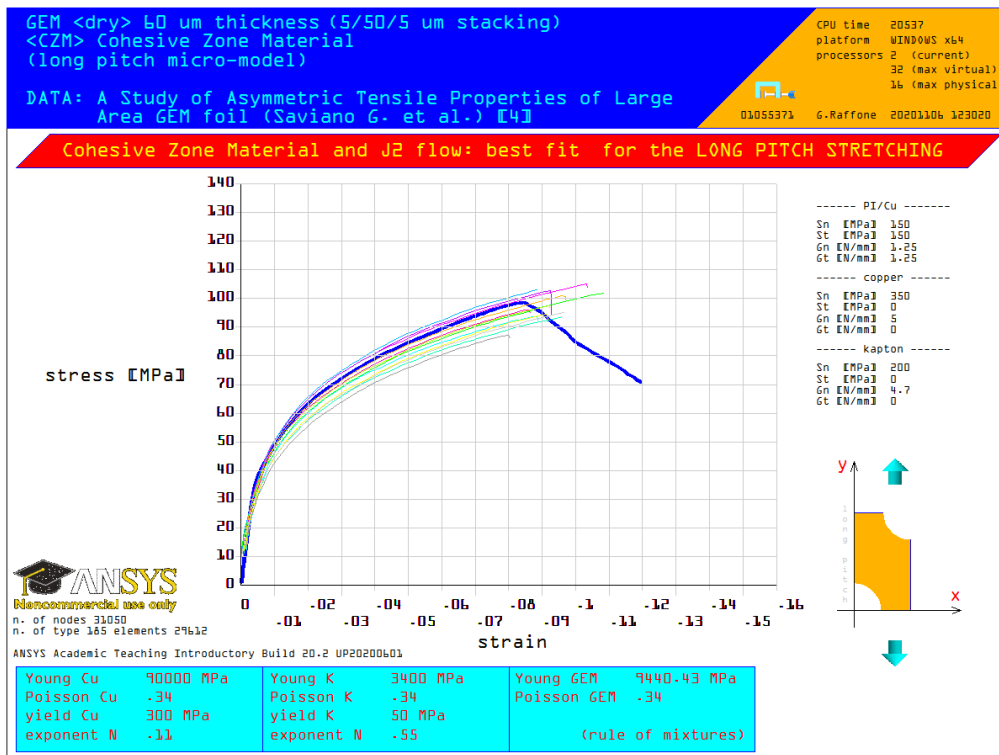


Figure 21: J2 and CZM load-stress curve for *long pitch* stretching; DATA points in [4].

¹⁸It is a common practice to assume $\sigma_{max}^I = \tau_{max}^I$ due to the lack of data for the PI/Cu interface.

¹⁹Some authors [18] assume the peak normal stress σ_{max}^f equal to the copper yield stress.

²⁰For instance a $0.8\mu\text{m}$ copper film fracture toughness is of the order of 7.8 MPam^{1/2} [27]; usually the fracture toughness scale with the thickness and is expected to be higher for much thicker films.

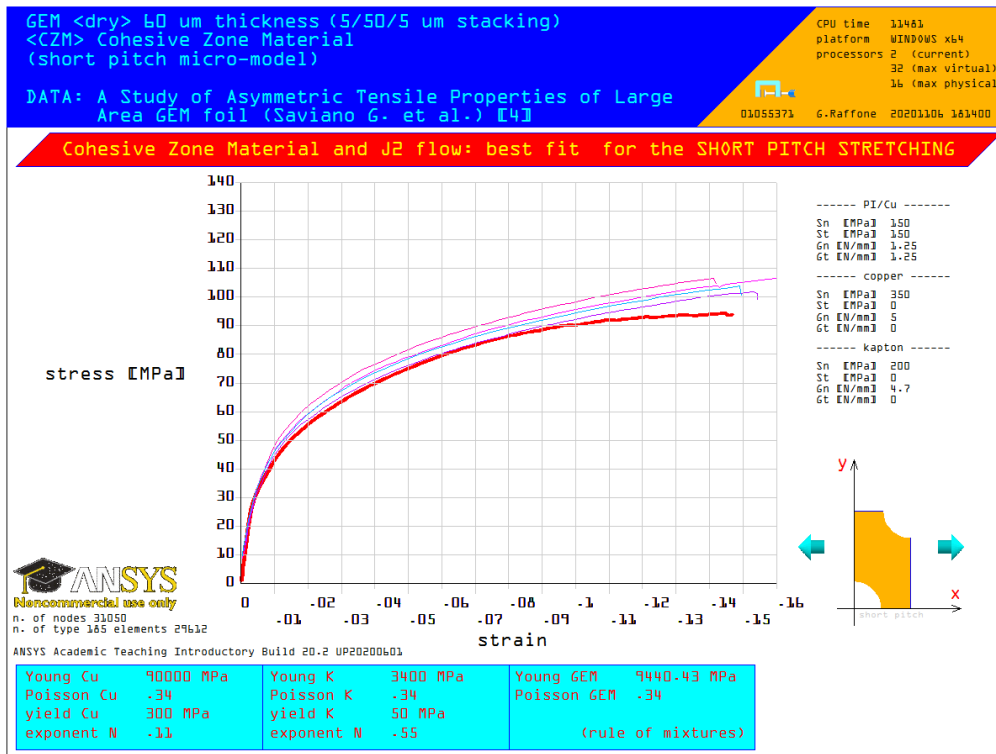


Figure 22: J2 and CZM load-stress curve for *short pitch* stretching; DATA points in [4].

Fig. 22 shows a very good agreement also for the *short pitch* stretching but the fracture is not fully developed yet at about 0.145 strain as expected and the load-strain curve follows some sort of *plateau*; indeed one of the four *REF* experimental curves [4] does not show any collapse up to 0.160 strain meaning that the tensile test ended at larger and larger strain; that *plateau* is indicative of a good Kapton® fracture toughness since at these strains the copper layer is almost detached leaving the substrate to carry all the tensile load alone; an analogous effect cannot be seen in the *long pitch* stretching because also the Kapton® layer suffers from the lower crack path length and survives only for a while after the copper detachment.

The fracture progression is greatly dissimilar (Fig.s from 23 to 27) and the absence of debonding up to the failure is the only common feature due to the applied strong PI/Cu interface. At the 0.005 strain the plasticization is already fully developed and the *short pitch* has still higher stress at $\pi/2$ than the *long pitch* at 0 because of the SCFs; nevertheless the *long pitch* is already in a worse condition since the plasticization is extended all over the path length while it is still confined in a small region for the *short pitch*; at 0.025 the crack, originated from the free surface of the copper, is growing in both cases but in the *long pitch* is already extended all over the path and the copper layer is close to the detachment while in the *long pitch* is only at the beginning; at higher strains the *long pitch* copper layer is detached and the crack is penetrating in the underlying Kapton® layer while the *short pitch* follows a classical channel crack evolution.

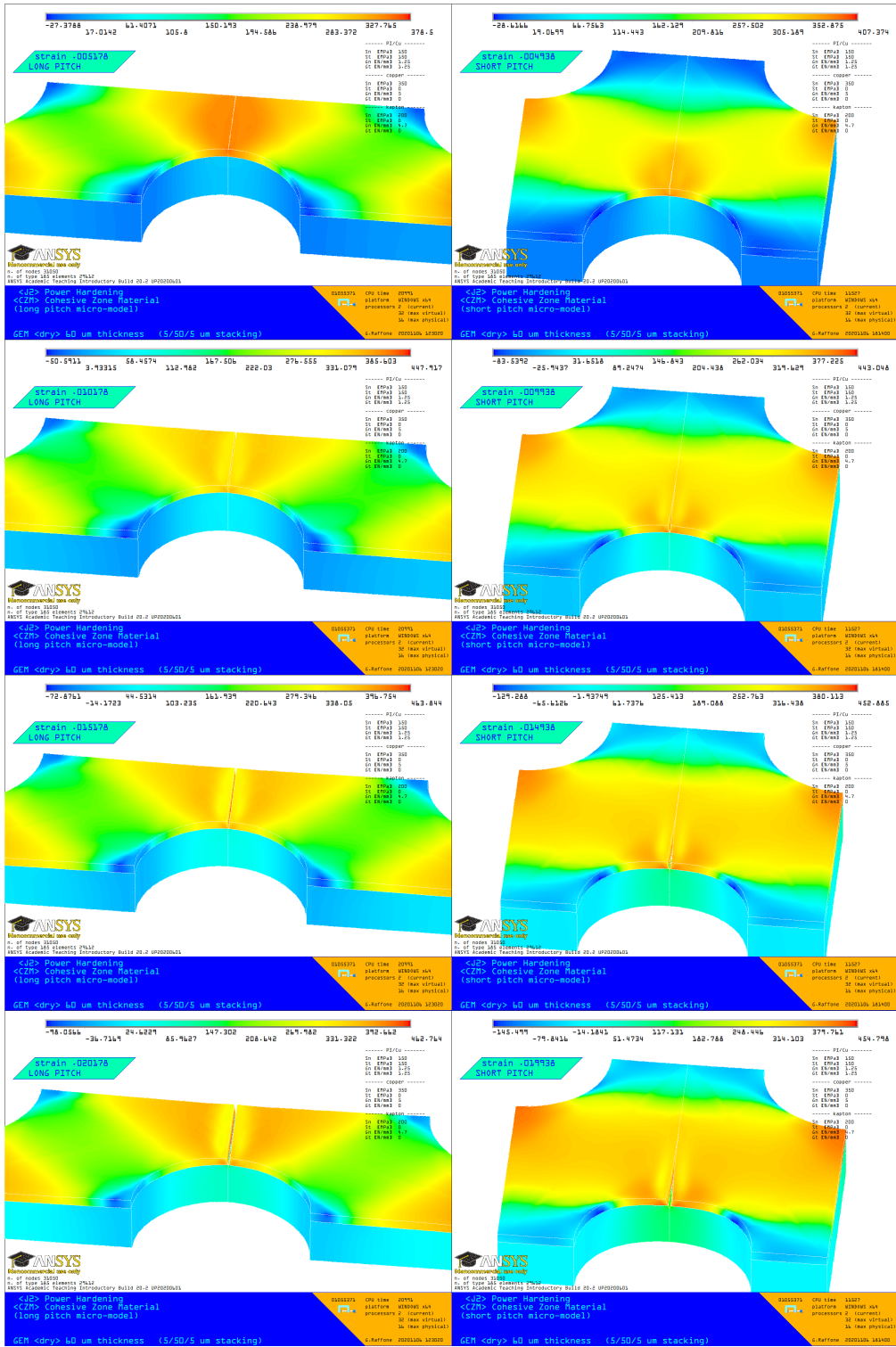


Figure 23: Crack propagation sequence from 0.005 to 0.020 strain.

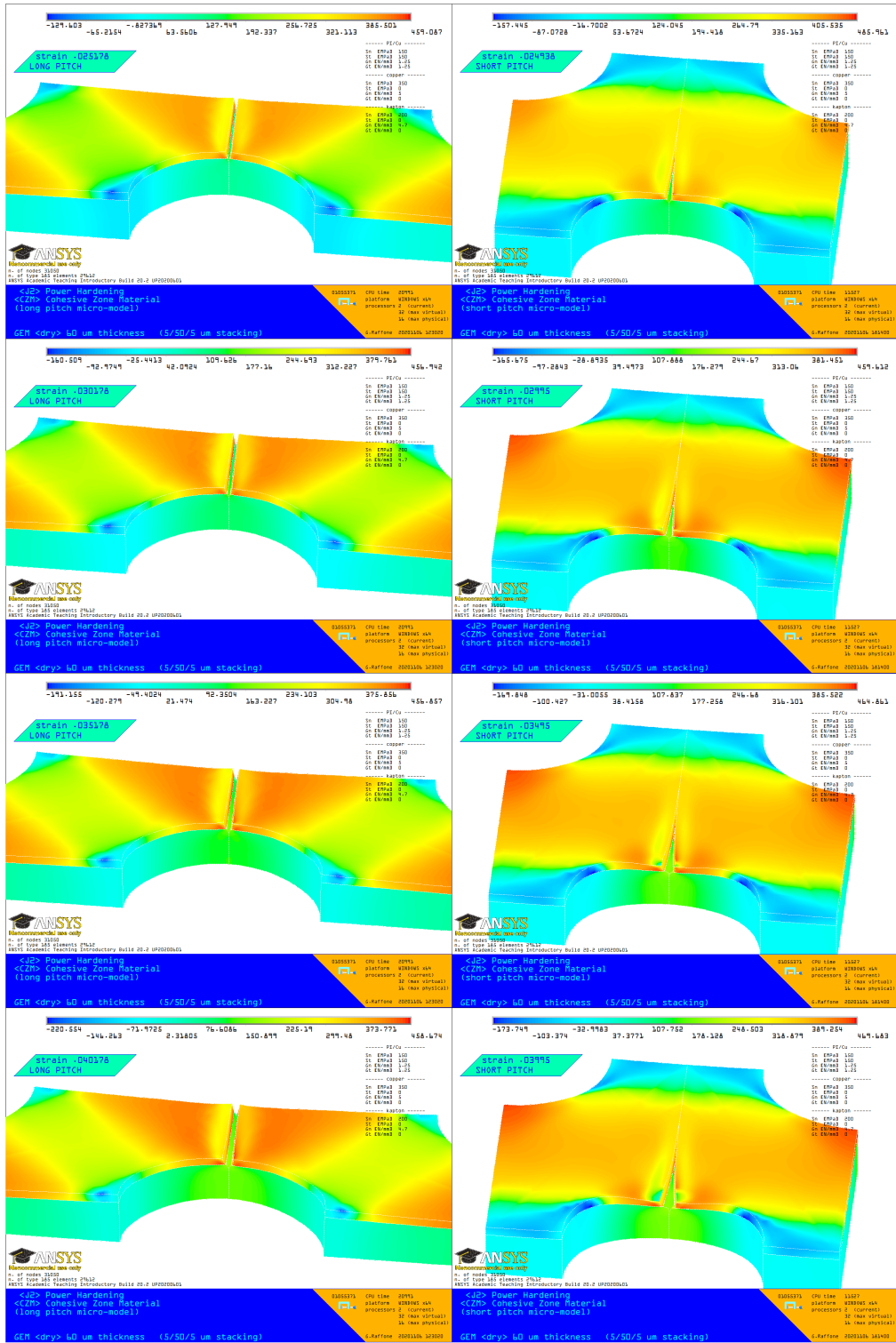


Figure 24: Crack propagation sequence from 0.025 to 0.040 strain.

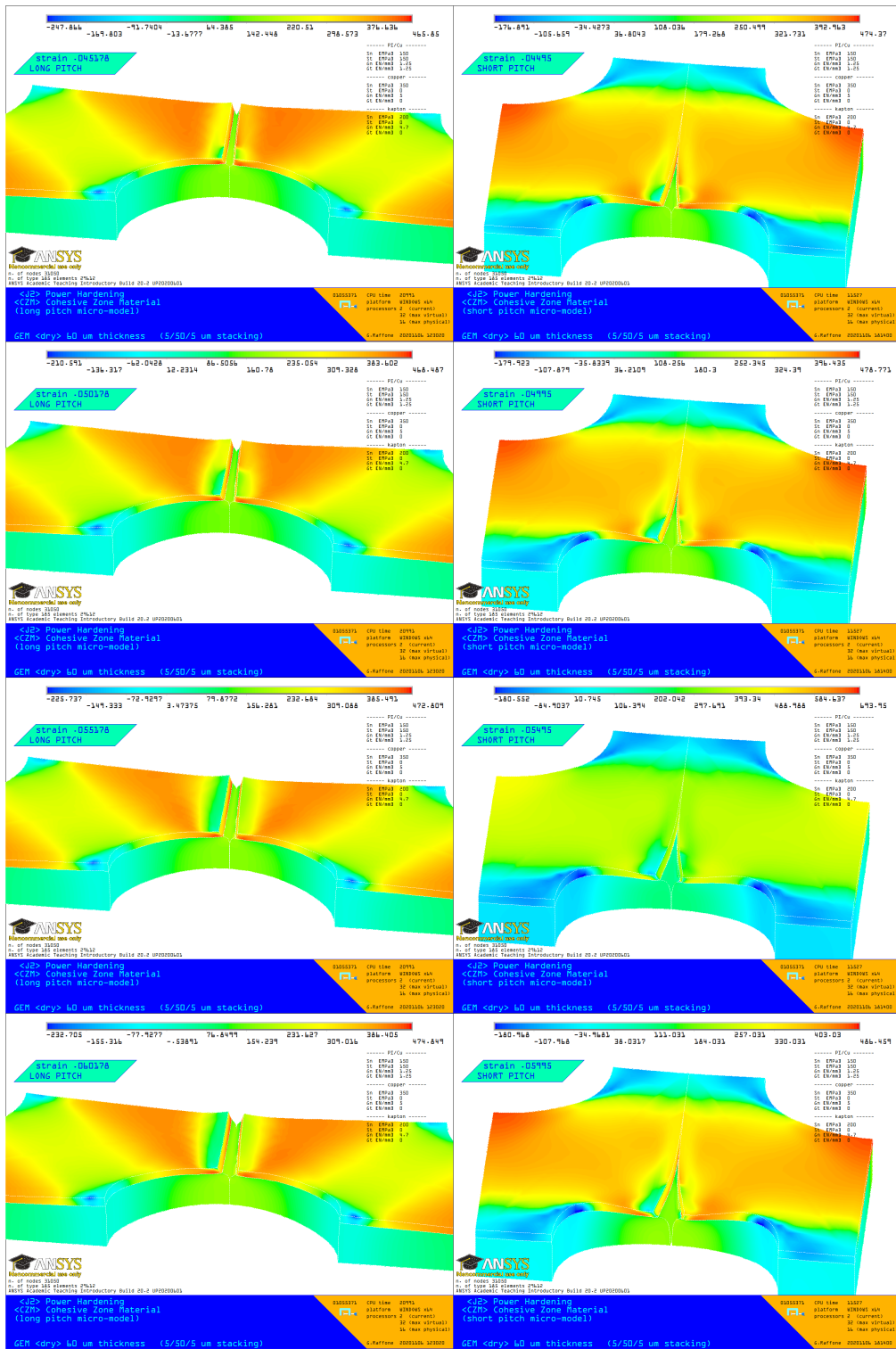


Figure 25: Crack propagation sequence from 0.045 to 0.060 strain.

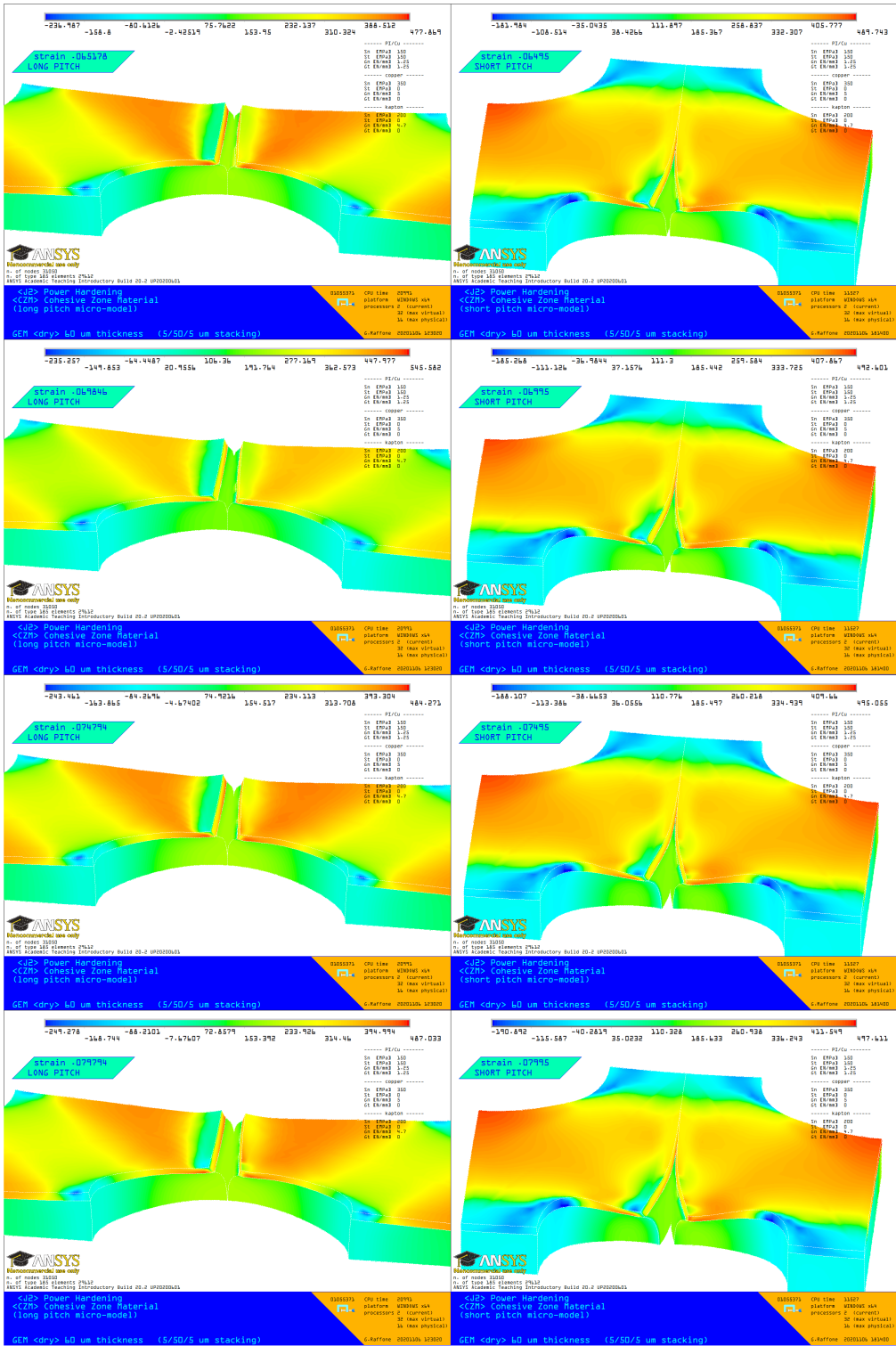


Figure 26: Crack propagation sequence from 0.065 to 0.080 strain.

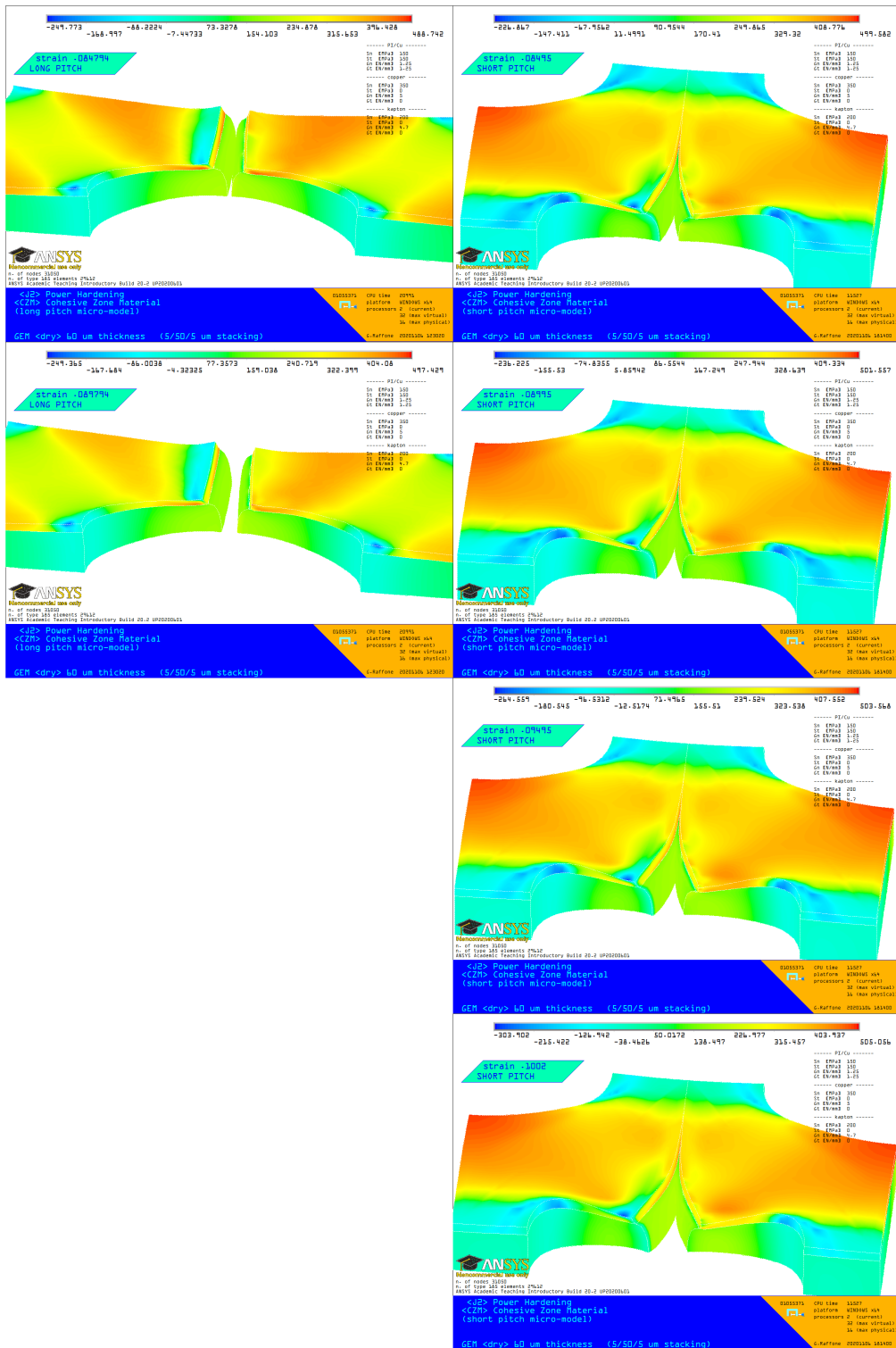


Figure 27: Crack propagation sequence from 0.085 to 0.100 strain.

A clear example of how the Kapton® layer and its adhesion drive the process is given by leaving unchanged the copper interface properties $\sigma_{max}^f = 350$ MPa and $\Gamma_{\sigma}^f = 5$ N/mm²¹ and setting $\sigma_{max}^s = 100$ MPa and $\Gamma_{\sigma}^s = 1.1$ N/mm for the Kapton® interface corresponding to a severe degradation of the polymer respect to the values assumed for the non-irradiated samples; also the PI/Cu interface is assumed to be greatly damaged than before setting $\sigma_{max}^I = \tau_{max}^I = 5$ MPa and $\Gamma_{\sigma,\tau}^I = 0.5$.

That set of parameters fits the load-strain curve of Fig. 28²² [3] showing the premature failure of some neutron irradiated GEMs samples that presumably are of the *long pitch* type due to their greater slope at low strain; it seems that the neutron radiation [6] probably degraded the mechanical properties of the Kapton® substrate of these samples more than others; the collapse happens approximatively at 0.03 strain and 67 MPa load and the agreement with Fig. 29 is very good.

Figs 30 and 31 show a comparison between the non-irradiated and the damaged samples sequences for the *long pitch* stretching; at 0.005 strain the stresses are the same but the damaged copper layer is *freestanding*, i.e. already debonded from the Kapton® substrate; at 0.010 strain the damaged copper layer is both detached and debonded while the substrate does not show any crack yet; the detachment and debonding go on till 0.025 strain when the fracture origins in the substrate that rapidly collapse at 0.030 strain. Of course that simulation, as the previous ones, is no more than an example of how the CZM model can be utilized not only to simulate but to understand such a complex plasticization process; at the same time that kind of approach must be fully supported by the experimental tests to become a real design tool rather than an academic exercise.

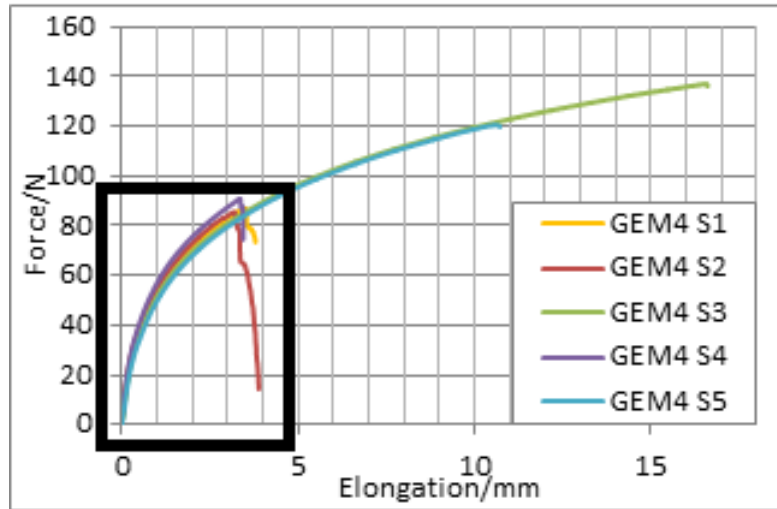


Figure 28: Premature failure of neutron irradiated GEMs (image edited courtesy of [3]).

²¹It is assumed that the neutron radiation damage of the copper film is negligible.

²²Divide force [N] by 1.2 mm² to have stress [MPa] and elongation [mm] by 100 mm to have strain.

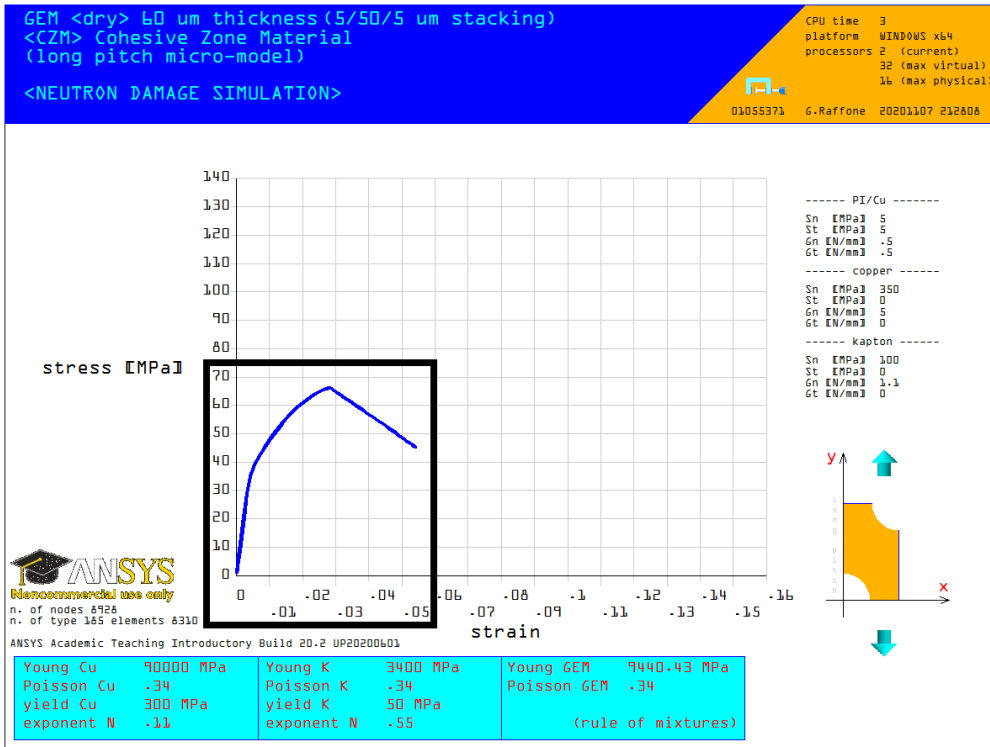


Figure 29: Severe degradation of the Kapton® and the PI/Cu interfaces.

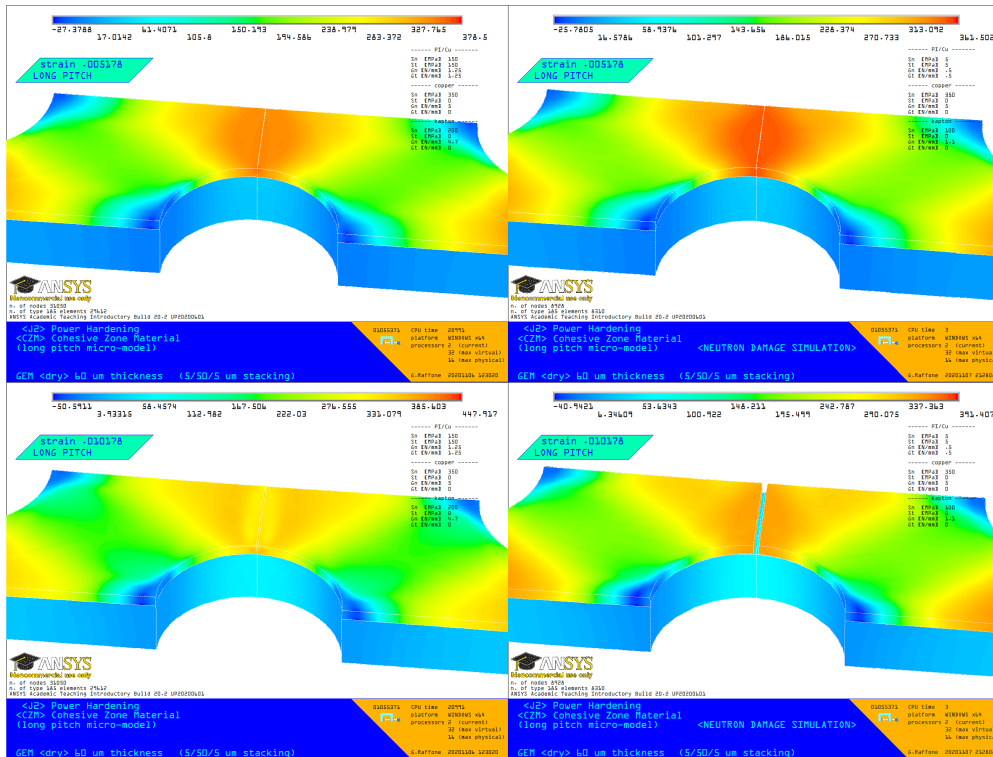


Figure 30: Crack propagation sequence from 0.005 to 0.010 strain (damaged).

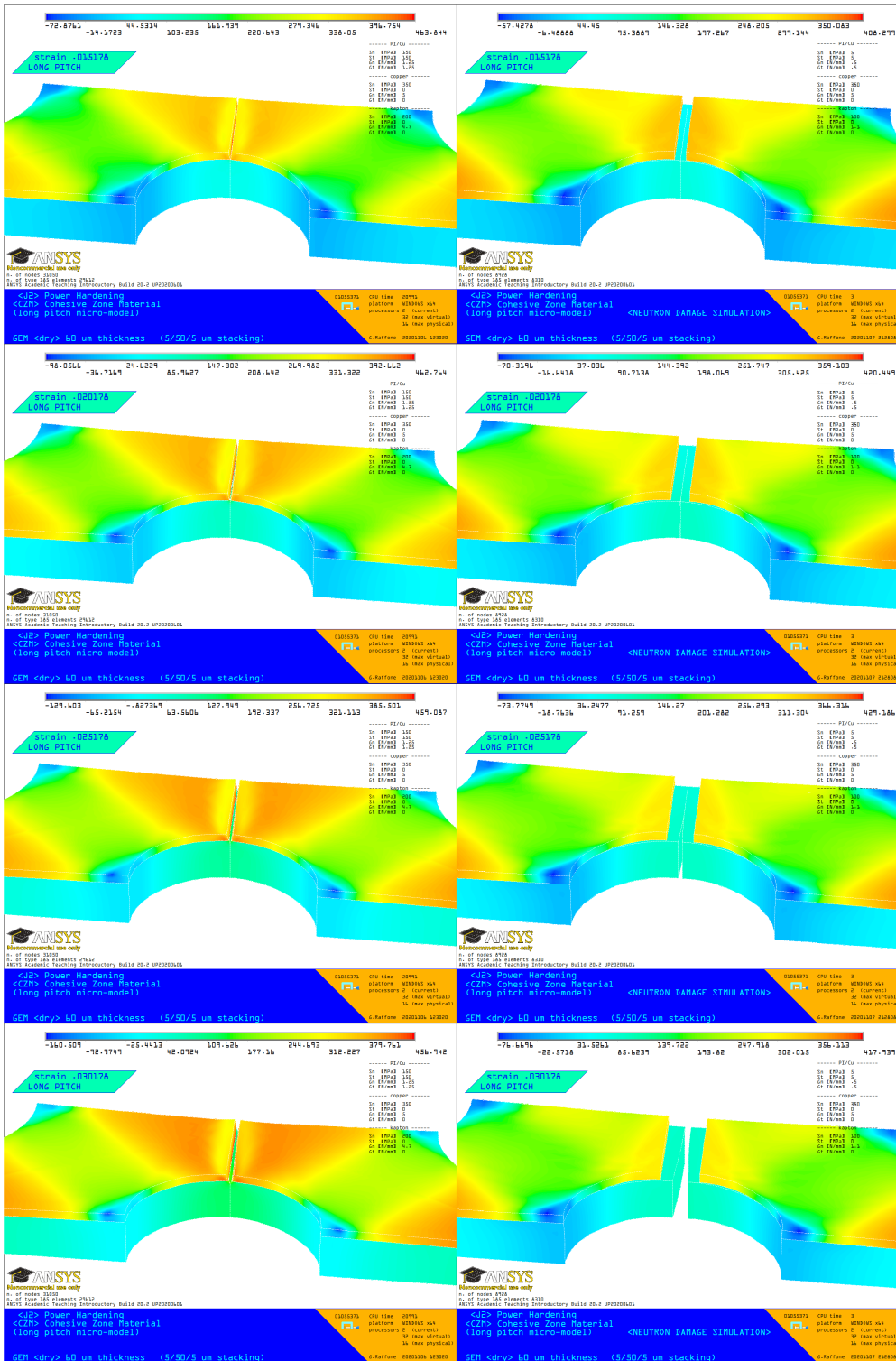


Figure 31: Crack propagation sequence from 0.015 to 0.030 strain (damaged).

4 Conclusions.

From structural point of view a GEM foil exhibits two kinds of asymmetry: a *geometrical* (*short* and *long pitch*) and a *mechanical* (*Stress Concentration Factors*); both these asymmetries contribute to the plastic evolution and to the final collapse of the specimens in uniaxial tensile tests with different weights and a mutual dependency; the numerically computed load-strain curves, the holes deformations as well as the failure strains agree very well with several experimental results and endorse that any other kind of asymmetry is not justified.

The FEM model [2] makes use of the *nonlinear isotropic power hardening* and the *cohesive zone material* [1] features whose parameters are mainly retrieved from literature since there is no experimental support for this kind of simulations; these parameters sometimes appear to be forced to utmost values in order to fit the experimental data; nevertheless that model describes extremely well the plasticity of the GEM foils and is also able to predict their premature failures for instance due to the neutron radiation damage presumably because of the degradation of both the Kapton® substrate and the PI/Cu bonding interface.

The assumption of the crack propagation perpendicular to the load direction seems to be too tight for the *short pitch* stretching leading to some sort of *plateau*; Fig. 32 shows an alternative lower energy crack path that should match the collapses at about 0.145 strain; that *zig-zag* path requires twice the size of the adopted FEM micro-model.

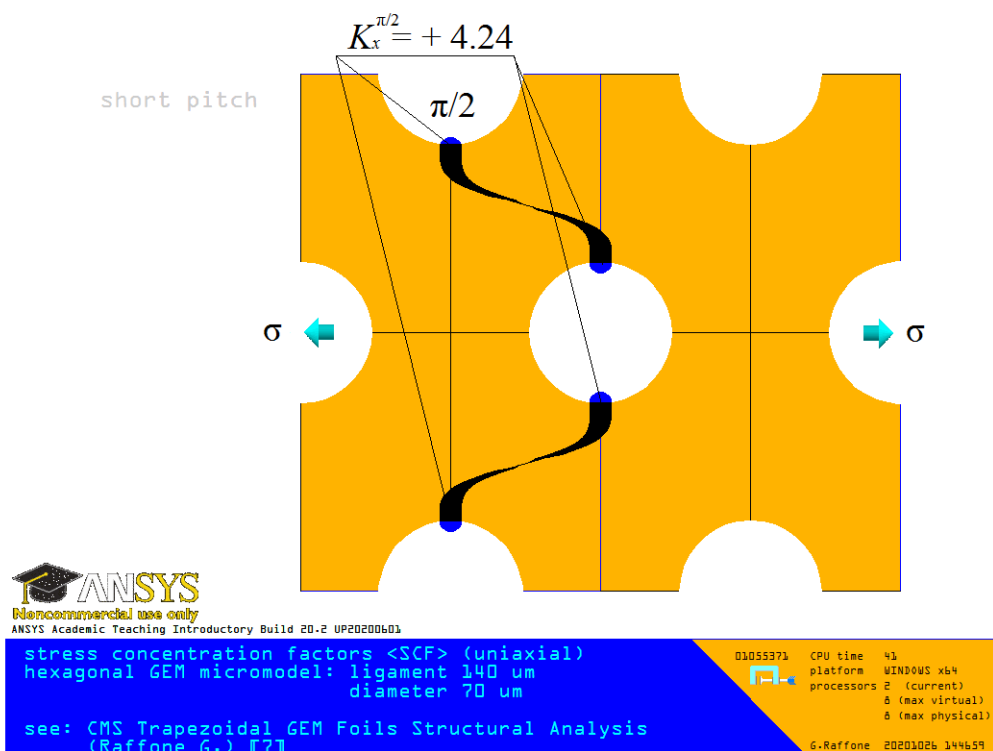


Figure 32: *zig-zag* crack path for the *short pitch* stretching.

References

- [1] Alfano, G. and Crisfield, M.A., *Finite element interface models for the delamination analysis of laminated composites: mechanical and computational issues*, [Int. J. Numer. Meth. Engng.](#), Vol. **50**, Issue 7 (2001), pages 1701-1736.
- [2] ANSYS® *Academic Teaching Introductory Build 20.2 UP20200601 (noncommercial use only)*, Copyright© 1994-2020 by ANSYS® Inc. as an unpublished work.
- [3] Benussi, L. *et al.*, *Gas Electron Multiplier foil holes: a study of mechanical and deformation effects*, [Journal of Instrumentation](#), Vol. **11** (2016).
- [4] Saviano, G. *et al.*, *A study of asymmetric tensile properties of large area GEM foil*, [Journal of Instrumentation](#), Vol. **15** (2020).
- [5] Abbaneo, D. *et al.*, *A study of film and foil materials for the GEM detector proposed for the CMS muon system upgrade*, [Journal of Instrumentation](#), Vol. **9** (2014).
- [6] Saviano, G. *et al.*, *A study of mechanical properties of foil materials for the GEM detector proposed for the CMS muon system upgrade at LHC*, [Polym. Eng. Sci.](#), Vol. **58**, Issue 9 (2018), pages 1539-1547.
- [7] Raffone, G., *CMS Trapezoidal GEM Foils Structural Analysis*, [LNF-10/20\(IR\) note](#), Laboratori Nazionali di Frascati, Frascati (RM), Italy (2010).
- [8] Sauli, F., *GEM: A new concept for electron amplification in gas detectors*, [Nucl. Instrum. Meth. A](#) Vol. **386**, Issue 2-3 (1997), pages 531-534.
- [9] Wikipedia contributors, *Gas electron multiplier*, [Wikipedia, The Free Encyclopedia](#), retrieved 19:12, October 20, 2020.
- [10] Macionczyk, F. and Bruckner, W., *Tensile testing of AlCu thin films on polyimide foils*, [Journal of Applied Physics](#) Vol. **86**, Issue 9 (1999), pages 4922-4929.
- [11] Rodriguez, C.A. *et al.*, *SOFA: a new approach for Quality Assurance in GEM foil*, [PoS](#), Vol. **ICHEP2016** (2017), pages 748-751.
- [12] Sun, J.Y. *et al.*, *Columnar grown copper films on polyimides strained beyond 100%*, [Scientific Reports](#), Vol. **5** N. 13791 (2015).
- [13] Yu, D.Y.W. and Spaepen, F., *The yield strength of thin copper films on Kapton*, [Journal of Applied Physics](#) Vol. **95** (2004), pages 2991-2997.
- [14] Xiang, Y. *et al.*, *The mechanical properties of freestanding electroplated Cu thin films*, [Journal of Materials Research](#), Vol. **21**, Issue 6 (2006), pages 1607-1618.

- [15] Lee, Y.S. *et al.*, *Structure-dependent mechanical behavior of copper thin films*, *Materials Characterization*, Vol. **128** (2017), pages 68-74.
- [16] Xiang, Y. and Vlassak, J.J., *Bauschinger and size effects in thin-film plasticity*, *Acta Materialia*, Vol. **54**, Issue 20 (2006), pages 5449-5460.
- [17] Li, T. *et al.*, *Competing failure mechanisms of thin metal films on polymer substrates under tension*, *Theoretical and Applied Mechanics Letters*, Vol. **1**, Issue 4 (2011).
- [18] Xu, W. *et al.*, *Effects of interfacial properties on the ductility of polymer-supported metal films for flexible electronics*, *International Journal of Solids and Structures*, Vol. **47**, Issues 1415 (2010), pages 1830-1837.
- [19] Li, T. and Suo, Z., *Ductility of thin metal films on polymer substrates modulated by interfacial adhesion*, *International Journal of Solids and Structures*, Vol. **44**, Issue 6 (2007), pages 1696-1705.
- [20] DuPont™ Kapton® HN Polyimide Film Data Sheet, PDF (2019).
- [21] O'Donnell, W.J. and Langer, B.F., *Design of Perforated Plates*, *ASME Journal of Engineering for Industry*, Vol. **84**, Issue 6 (1962), pages 307-319.
- [22] Staib M., *et al.*, *Thermal Stretching of Large-Area GEM Foils Using an Infrared Heating Method*, *RD51 Technical Note 004* (2011).
- [23] Xiang Y., *et al.*, *High ductility of a metal film adherent on a polymer substrate*, *Appl. Phys. Lett.*, Vol. **87**, 161910 (2005).
- [24] Walter, T. *et al.*, *Delamination of polyimide/Cu films under mixed mode loading*, *Microelectronics Reliability*, Vol. **64** (2016), pages 281-286.
- [25] Hinkley, J.A. and Mings, L., *Fracture toughness of polyimide films*, *Polymer*, Vol. **31**, Issue 1 (1990), pages 75-77.
- [26] Min, H.G *et al.*, *Comparison of Tensile and Fatigue Properties of Copper Thin Film Depending on Process Method*, *Appl. Sci.*, Vol. **10**, Issue 1 (2020), 388.
- [27] Hirakata, H. *et al.*, *Size effect on fracture toughness of freestanding copper nano-films*, *Material Science and Engineering: A*, Vol. **528**, Issue 1 (2011), pages 8120-8127.